# Poromechanical analysis of oil well cements in CO2-rich environments

**Barría, J. C., Bagheri, M., Manzanal, D., Shariatipour, S. M. & Pereira, J. M**



DOI 10.1016/j.ijggc.2022.103734
ISSN 1750-5836

Publisher: Elsevier

International Journal of Greenhouse Gas Control 119 (2022) 103734

Contents lists available at ScienceDirect

International Journal of Greenhouse Gas Control

journal homepage: www.elsevier.com/locate/ijggc

# Poromechanical analysis of oil well cements in $CO_2$-rich environments

Juan Cruz Barría [a,b], Mohammadreza Bagheri [c], Diego Manzanal [d,*], Seyed M. Shariatipour [c], Jean-Michel Pereira [b]

[a] Engineering Faculty, Universidad Nacional de la Patagonia (UNPSJB), Ciudad Universitaria, RPN° 1 Km4., Comodoro Rivadavia, Chubut 9004, Argentina
[b] Navier, Ecole des Ponts, Univ Gustave Eiffel, CNRS, Marne-la-Vallée, France
[c] Research Centre for Fluid and Complex Systems, Coventry University, Mile Lane, Coventry CV1 2NL, UK
[d] Mecanica de Medios Continuos y Teoría de Estructuras, Universidad Politecnica de Madrid Escuela Tecnica Superior de Ingenieros de Caminos Canales y Puertos, Ciudad Universitaria, Av. Prof. Aranguren 3, Madrid 28040, Spain

ARTICLE INFO

*Keywords:*
Supercritical carbonation
Class G cement
Poromechanical behavior
Numerical modeling

ABSTRACT

Wells drilled in carbon storage sites could be converted to potential leakage pathways in the presence of $CO_2$-bearing fluids and under the impact of the changes occurring in underground stress. To test this hypothesis, in this study, the behavior of Class G oil well cement in contact with supercritical $CO_2$ has been investigated. The cement cores were cured under lime-saturated water for 28 days at a temperature of 20 °*C* and under atmospheric pressure. Subsequently, they were exposed to supercritical $CO_2$ under a pressure of 20 MPa and at a temperature of 90 °*C* for 30 days. The penetration depth of the carbonation front and the change in the poromechanical properties of the cement core were measured against time. A numerical modeling exercise has also been conducted to simulate the alteration within the cement cores. The results presented in this study show that the precipitation of calcium carbonates reduces the porosity within the outermost layers of the cement cores. This phenomenon shifts the main pore size class towards smaller sizes. In contrast to expectations, the reduction in porosity does not improve the overall strength of the cement specimens. The observed reduction in the strength of the cement specimens might be associated with either the amorphous structure of the precipitated carbonates or the weak bonding between them and the solid walls of the pores and the high degradation of calcium silicate hydrates.

## 1. Introduction

Reducing fossil fuel consumption and replacing it with nuclear or renewable energy is the next step in decreasing greenhouse gas emissions. In the meantime, carbon capture and storage (CCS) has become one of the most important solutions to reduce these emissions (Lokhorst and Wildenborg, 2005). This technology can be applied to former oil reservoirs to take advantage of the drillings and pipes already installed and benefit from the extensive data available. The ways to reach new reservoirs in the context of CCS are similar to the oil industry practice. It consists of drilling to the reservoir and assuring the integrity of the well by placing a steel casing inside the wellbore and cementing the annular section between them.

The hardened cement paste aims at maintaining the integrity of the casing-cement-wellbore system by filling the gaps between the casing and the geological formations. It improves the mechanical performance of the well and also protects the casing from corrosive formations fluids. Moreover, the cement sheath must assure zonal isolation to prevent fluid migration (Gasda et al., 2004).

The reservoir capacity to store carbon dioxide ($CO_2$) substantially improves if the temperature and pressure conditions maintain $CO_2$ in a supercritical state (Ringrose, 2020). Under these conditions, the density of the fluid increases and has a viscosity such as a gas. Cement is a multiphase material mainly composed of Portlandite (CH), calcium silicate hydrates (C-S-H), and aluminates in the form of ettringite ($AF_t$) and monosulphoaluminate ($AF_m$). C-S-H is the most influential material in cement mechanical behavior. Cement strength can be affected by several factors during the carbonation process. Once C-S-H starts degrading, the cementitious matrix also begins dissociating which results in modifying the stress distribution and strength. This phenomenon occurs because the hydrated compounds in the cement matrix are replaced by other phases which are less strong, such as amorphous silica (AS), and less cohesive.

The dissolution of $CO_2$ in brine as a ubiquitous phase within the

* Corresponding author.
*E-mail address:* d.manzanal@upm.es (D. Manzanal).

https://doi.org/10.1016/j.ijggc.2022.103734
Received 9 November 2021; Received in revised form 10 June 2022; Accepted 12 July 2022
Available online 25 July 2022

pores of the cement matrix reduces its pH from around 13 to less than 4 (Duan and Sun, 2003; Taylor, 1997). CH easily dissolves in $CO_2$-bearing fluids prior to C-S-H (Glasser and Matschei, 2007; Kutchko et al., 2011). However, it has been observed that the carbonation of CH and C-S-H decalcification can occur simultaneously (Kutchko et al., 2011; Liaudat et al., 2018). The products of the stoichiometric balances are calcium carbonates (CC) and water for the CH reagent, while for the C-S-H+ $CO_2$ balance, CC and AS are the generated products (Fernández Bertos et al., 2004). The dissolution of C-S-H generally leads to a decrease in the Ca/Si ratio from 2.0 to around 0.8 (Carey, 2013; Liaudat et al., 2018; Trapote-Barreira et al., 2014). The dissolution of C-S-H is not proportional to the stoichiometric coefficients. This implies that the composition of C-S-H changes during the dissolution process. It was shown that C-S-H incongruently dissolves at high Ca/Si ratios (preferential Ca release compared to Si) and congruently by decreasing the Ca/Si ratio (this ratio reaches a steady state) (Trapote-Barreira et al., 2014). The carbonation of CH begins once it is exposed to $CO_2$-bearing fluids, while C-S-H carbonation gradually increases with a drop in the pH value.

Four main zones are expected to be formed due to the invasion of $CO_2$-bearing fluids into a cement matrix, including the intact zone, CH dissolution zone, CC precipitation zone, and the silica gel zone, from the inner parts of the cement matrix towards its outermost layers, respectively (Carey et al., 2010; Choi et al., 2016; Corvisier et al., 2013, 2010; Iyer et al., 2017; Kutchko et al., 2007; Kutchko et al., 2008; Liaudat et al., 2018; Omosebi et al., 2016; Rimmelé et al., 2008b).

Carbonate anions react with calcium cations diffusing towards the outermost layers of the matrix. This reaction leads to the precipitation of CC. This area is referred to as the CC precipitation zone (Carey, 2013; Corvisier et al., 2010; Wigand et al., 2009). The alteration of C-S-H and the depletion of CH, particularly within the areas adjacent to the cement-brine interface leave behind the AS gel (Duguid and Scherer, 2010; Walsh et al., 2013). It was observed that the carbonation shrinkage of C-S-H produces cracks (Auroy et al., 2015). Furthermore, the growth of CC crystals within a pore can generate volumetric tensile stresses, which can exacerbate the damage to the cement matrix (Manzanal and Pereira, 2013). Two studies showed severely damaged samples where a detachment of layers around the sample was observed (Rimmelé et al., 2008a) .

The term degradation is generally used for describing the re-dissolution of CC and AS gel (Bagheri et al., 2018; Zhang and Bachu, 2011). CC and the remaining C-S-H re-dissolve in the presence of more $CO_2$-bearing fluids invading the outer face of the cement matrix. This process is sometimes referred to as bicarbonation (Zhang and Bachu, 2011).

The physical changes during carbonation lead to a variation in porosity due to the difference between the molar volumes of the products and those of the reactants. Initially, the porosity within the calcium precipitation zone decreases because the molar volume of CC is higher than CH (Barlet-Gouédard et al., 2007). As the carbonation reaction progresses inwards in the cement core, the degradation of C-S-H continues, and gel pores consequently start growing due to C-S-H decalcification. Shen et al. (Shen et al., 2016) quantified that C-S-H degradation contributes up to 70% in the total variation in porosity.

Potential clogging due to precipitated CC is a function of the initial porosity, CH fraction, and the residence time of the carbon species on the surface of the cement matrix (Asahara et al., 2013; Brunet et al., 2016, 2013; Cao et al., 2013; Huerta et al., 2016; Iyer et al., 2017). A study by Brunet et al. (Brunet et al., 2013) showed that for a diffusion-controlled process, no clogging is expected to occur within low-Portlandite and high-porosity cement matrices. Conversely, the clogging tendency increases for high-Portlandite and low-porosity cement matrices. With increasing residence time, the degradation intensity decreases due to the consumption of carbon species in the reactions. This process can result in the self-healing of the cracks. Cao et al. (Cao et al., 2013) introduced a threshold in their model to discriminate between the self-healing and the self-opening behavior of the cracks. They showed that with increasing the residence time, the chance of clogging increases due to the precipitation of CC. With decreasing residence time, CC will not precipitate within the cement cracks.

The permeability of a cement matrix is linked to its porosity, how the pores are interconnected, and the direction of the corresponding flow (Bagheri et al., 2018). Lesti et al. (Lesti et al., 2013) observed this effect on samples carbonated six months under wet supercritical $CO_2$. Porosity was reduced from 22% to 14%, while the gas permeability increased from 0.1 nD to 1.54 μD. This increase in permeability is attributed to the crack formation in the cement matrix due to C-S-H shrinkage caused by its decalcification and the pore expansion caused by the crystallization of $CaCO_3$ during carbonation (Auroy et al., 2015; Lesti et al., 2013; Manzanal and Pereira, 2013). On the other hand, Bachu et al. (Bachu and Bennion, 2009) saw a reduction in the permeability to brine from 0.25 μD to 10 nD, suggesting that there is a threshold for the pressure drop that should be considered when using gas or brine permeabilities. This difference in permeabilities is related to the mode of fluid transport within the pores. The gas molecules can pass through smaller pores, which can be generated by the decalcification of C-S-H and leads to an increase in its gas permeability. This increase in smaller pores quantity was observed by Barría et al. (Barría et al., 2022), where the capillary porosity (allows the passage of fluids, d>10 nm) of the cement decreased while the gel porosity (the pores within the structure of the hydration product, d<10 nm) showed an increase after 120 days of carbonation. However, more studies are required to confirm this conclusion. Furthermore, the increase in permeability can also be influenced by the re-dissolution of the carbonation front, which may lead to an increased porosity (Zhang and Bachu, 2011).

In many experiments, the static conditions are preferred to the flow-through conditions (Corvisier et al., 2013, 2010; Kutchko et al., 2009; Rimmelé et al., 2008b; Zhang et al., 2013). This is due to the low velocity of $CO_2$-bearing fluids in the vicinity of abandoned wells. In this case, the kinetics of the reactions are faster than the diffusion process (Huet et al., 2006). Thereby, the evolution of the cement matrix will be dominated by the diffusion process, which justifies the application of batch experiments (Kutchko et al., 2009; Rimmelé et al., 2008b). Indeed, it is the pressure conditions and the geometry of the leakage pathway which dictate whether static or dynamic conditions are relevant in a given application. The use of batch experiments limits to conditions when the time scale of advection is longer than the diffusion time scale.

The duration of experiments imitating the exposure of the cement to $CO_2$-bearing fluids is not comparable to the real-life of oil well cement. Numerical modeling provides this opportunity to extrapolate the experimental data for predicting the performance of the oil well cements in $CO_2$-rich environments (Zhang et al., 2013). Such a numerical study emphasizes diffusion-based modeling because the static condition dominates the experiment. The depth of the carbonation front, $d$, is modeled as a linear diffusion, $d = k\sqrt{t}$, where $t$ is time, and $k$ is a constant which depends on the relative humidity, water saturation, cement type, $CO_2$ concentration, and other surrounding conditions (Ashraf, 2016; Phung et al., 2016; Rezagholilou et al., 2017; Šavija and Luković, 2016; Silva et al., 2014; Ta et al., 2016). However, more complicated models were also developed for predicting the depth of carbonation front (Corvisier et al., 2013; Huet et al., 2006).

A sequential iterative approach was used by Huet et al. (Huet et al., 2010) to couple the geochemical alteration with the transport process to model the aqueous phase speciation, the porosity-dependent transport properties, and mineral precipitation/dissolution. Their model was able to qualitatively reproduce the experimental results reported by Duguid (Duguid et al., 2005). However, they modified the relationship between the porosity and the effective diffusivity to obtain a match between the modeling results and the experimental data. A modeling study was conducted by Brunet et al. (Brunet et al., 2013) in which the cementation factor (it describes the relationship between the porosity and effective diffusion coefficient) was identified as the most critical

parameter controlling the cement alteration in $CO_2$-rich environments. In this study, the same as (Huet et al., 2010), the effective diffusion coefficient was recognized as the limiting part of the simulation. The experimental data in (Duguid and Scherer, 2010) were regenerated by Liaudat et al. (Liaudat et al., 2018). They indicated that the penetration depth can be quantitatively modeled if the change in the effective diffusivity due to the degradation process is accounted for.

The behavior of the cracked cement matrices exposed to $CO_2$-bearing fluids is examined in the presence of a confining pressure in (Walsh et al., 2014). It was shown that the hydraulic fracture aperture decreases due to the synergy between the weakening effect of geochemical reactions and the confining pressure. The AS gel layer was shown to be the most compressible zone. It was observed that the precipitation of CC leads to an increase in the cement strength within this zone to equal or just above that for the intact zone (Walsh et al., 2014). The CH dissolution provides more pore space for the solid phase expansion during the plastic dilation, which results in the failure delay (Ulm et al., 2003). On the other hand, the dissolution of C-S-H leads to chemo-mechanical softening, which can be modeled using chemoplasticity (Coussy and Ulm, 1996). Fabbri et al. (Fabbri et al., 2009) reported that the cores with annular carbonation are more sensitive to stress compared to the cement cores, which are homogeneously carbonated. In their study, it was observed that the cement cores with the annular carbonation were damaged more than the homogeneously carbonated cement ones. They interpreted this issue as a result of the extension of microcracks around the carbonation fronts. In their experiments, this phenomenon led to a decrease in mechanical strength.

Fabbri et al. (Fabbri et al., 2009) measured the dynamic and static elastic constants and permeability of the Portland cement samples carbonated under wet supercritical $CO_2$ at 90 $^{\circ}C$ and 28 MPa. They observed an increase in the pressure sensitivity of samples with a developed carbonation front. They attributed this observation to the mechanical degradation and, consequently increased permeability within zones near the front. Wolterbeek et al. (Wolterbeek et al., 2016) undertook triaxial compression tests on Class G Portland cement at a temperature of 80 $^{\circ}C$ and the effective confining pressure in the range of 1-25 MPa. After that, the samples with localized shear fractures were exposed to $CO_2$-$H_2O$. Then their mechanical properties were measured again. It was observed that the reaction with $CO_2$ has no further degrading effect. Instead, they reported a recovery up to 83% in the peak strength. They also a 10-40% recovery for the frictional strength in the post-failure regime. It was represented that this recovery is attributed to the carbonated precipitation. Therefore, they claimed that self-healing could be the governing phenomenon for fractured cement. Mason et al. (Mason et al., 2013) ran an experiment in which $CO_2$-rich brine flowed through a small gap between the caprock and cement at a temperature of 60 $^{\circ}C$ and 3 MPa. They showed that the average Young modulus of depleted, carbonate, and amorphous zone decreased to about 75, 65, and 34% of that for intact zones. It was concluded by Mason et al. (Mason et al., 2013) that mineral dissolution and a consequent increase in porosity lead to a reduction in elastic modulus. To reveal the alteration of the mechanical properties of Class G Portland cement, scratch-hardness tests were conducted on cement samples before and after being exposed to $CO_2$. It was found that the brittle strength of each zone is approximately dependent on the exposure time and differences in each zone. An increase in the UCS of the carbonated zone was observed while this value reduces in porous silica zone compared to unreacted cement zones. Mason et al. (Mason et al., 2013) observed that the UCS increases by 1.5-3. Li et al. (Li et al., 2015) demonstrated that the hardness and indentation modulus in the carbonated layer increase by a factor of 2-3. This value is approximately halved within the Portlandite dissolution zones. They represented that the overall strength and the elastic modulus of the cement matrix decrease to 84% and 93% of their initial values, respectively. Investigating the alteration of the well cements exposed to $CO_2$-rich fluids is a crucial prerequisite for performing a safe CCS project. This is of great importance to predict the simultaneous effects of the geochemical reactions and the burdened stresses on the behavior of the cement matrix. It is an almost intact field of study in CCS which requires more attention. Thereby, this paper also tries to help widen the perspective to the complicated nature of the cement matrices in $CO_2$-rich environments.

In this paper, the behavior of Class G oil well cement is investigated in a $CO_2$-rich environment. The cement cores are exposed to supercritical $CO_2$ fluids in a high-pressure and high-temperature (HPHT) vessel. This work aims to contribute to the knowledge about the cement behavior at the macroscale when it is purely subjected to a supercritical carbonation process, focusing on its poromechanical behavior. This is particularly important in the context of $CO_2$ storage because the failure of the cement sheath could provide high leakage pathways. The penetration depth of the carbonation front and the mechanical properties of the cement cores are measured prior to and after exposure to supercritical $CO_2$ fluids. The cement matrix's pore size distribution (PSD) is measured using Mercury Intrusion Porosimetry (MIP), and the mechanical strength is measured by the uniaxial compressive strength apparatus. X-ray diffraction analysis (XRD) was performed on carbonated samples. Numerical modeling has also been conducted to explore the alteration in the geochemical and mechanical properties of the cement matrix. The results of this study help to develop the comprehension of the cement alteration in $CO_2$-rich environments.

## 2. Materials and methods

### 2.1. Experimental procedures

Cylindrical specimens of Class G cement were considered for the experiments. The samples were carbonated at 20 MPa and 90°C for 30 days. Mercury intrusion porosimetry, compressive strength tests, and X-ray diffraction analysis were performed on these specimens.

#### 2.1.1. Specimens preparation

Eight cylindrical specimens of 38 × 76 mm (diameter × length) of Class G oil well cement were made with a water to cement ratio (w/c) of 0.44. The slurry was poured into cylindrical molds in two layers, each layer being compacted with a puddling rod 27 times (API Specification 10A, 2019). Samples were cured for 24 h in a 20°C batch and unmolded. After removing them from the mold, they were kept under lime-saturated water for 28 days at room conditions (Barría et al., 2020, 2021a, 2021b). A long curing time was considered to reduce the impact of the hydration process that would otherwise occur during the carbonation stage. Indeed, these conditions were selected to characterize the sole effects of carbonation on a Class G cement.

#### 2.1.2. Carbonation

The carbonation tests were performed in a 16 × 20 cm cylindrical reactor under wet supercritical $CO_2$ at 20 MPa and 90°C for 30 days (Barría et al., 2021a, 2022). After sealing the cell, the pressure of carbon dioxide in the vessel was increased to 8 MPa. Then, the temperature was increased to 90°C. Following this, the $CO_2$ pressure was increased to 20 MPa by employing a pump. Samples were fully saturated before placing them in the reactor and water was poured at the bottom of the vessel to maintain humidity. With these conditions, the penetration of $CO_2$ in cement can be considered to occur through diffusion. The final pressure-temperature conditions and the path followed assured that the water remained in a liquid state. Additionally, the path followed assured that $CO_2$ passed from a liquid state to the supercritical state without passing through the gas state. Following the carbonation process, the heating was turned off, and the cell was allowed to reach room temperature. Afterward, the pressure was decreased until it reached ambient pressure. The weight of the specimens was measured before and after carbonation to obtain the mass uptake and the variation in their density.

#### 2.1.3. Characterization tests

The porosity and pore size distribution of the samples were measured employing a Mercury Intrusion Porosimeter (MIP). The equipment used was a Micromeritics AutoPore IV 9500. This instrument is capable of detecting pore sizes from 5 nm to 300 μm. The cylindrical specimens were crushed to obtain 0.5–0.6 g pieces and dried using freeze-drying prior to the measurement. The device measures the volume of mercury intruded into the sample per unit of mass with each step of pressure applied up to 230 MPa. Mercury intrudes interconnected porosity, so the isolated pores are not observable. To obtain the MIP porosity, the following expression is applied:

$$\phi = \frac{V_I}{V_T}\, m \tag{1}$$

where $V_I$ is the volume of intruded mercury per unit of mass of cement, $m$ is the mass of the sample, and $V_T$ is the total volume of the sample, which is obtained from the apparent density and the sample mass.

A hydraulic press with electronic vertical displacement and applied force measurement was used to perform the compression strength tests. Three specimens were tested to determine their mechanical performance before and after carbonation. The test speed was set at 0.5 mm/min.

XRD analysis was performed on a Philips 3020 diffractometer using CuKα radiation with a Ni-filter (35 kV, 40 mA). The method described by Moore and Reynolds [34] was followed for identification, while quantification was calculated based on the work of Biscaye [35]. Scanning was performed for angles between 3° and 70°, with a step of 0.04° and a count time of 2 s/step. No monochromator was used, and the openings were 1° for divergence, 0.2° for the reception, and 1° for dispersion. The samples analyzed were taken from non-carbonated specimens (Non-carbonated) and after 30 days of carbonation and near the exposed edge (Carbonated).

### 2.2. Numerical modeling

This section provides a review of the numerical modeling of the cement alteration.

#### 2.2.1. Geochemical modeling

The geochemical alteration of the cement matrix can be modeled by coupling the momentum, mass, and energy balance equations governing the reactive transport of fluids within their pores. The exposure of the cement matrix to $CO_2$-bearing fluids is accompanied by the advection process, the diffusion process, and geochemical reactions that govern the mass balance. By considering the dominant phenomena in a fluid phase $\beta$, the following equation can be derived for the mass conservation of the component $j$ in an arbitrary cell within a $CO_2$ storage site (Ajayi and Gupta, 2019; Steefel et al., 2015):

$$\frac{\partial\left(\phi S_\beta C_{j_\beta}\right)}{\partial t} = \nabla.\left(\phi S_\beta D^*_{j_\beta}\nabla C_{j_\beta}\right) - \nabla.\left(q_\beta C_{j_\beta}\right) + R_{j_\beta} + \zeta_{j\beta} + S_{j_\beta},\ (j = 1, 2, 3, \ldots n) \tag{2}$$

where $j$ refers to the components in the phase $\beta$, $\phi$ is the porosity, $S_\beta$ is the saturation of phase $\beta$, $C_{j_\beta}$ $(mol/m^3)$ is the concentration of the component $j$, $q_\beta$ $(m/s)$ is the velocity of the phase $\beta$, $D^*_{j_\beta}$ $(m^2/s)$ is the diffusion coefficient of the component $j$ in the porous medium, $R_{j_\beta}$ $(mol/(m^3.s))$ is the summation of the produced and the consumed concentration over time for the component $j$. The term on the left-hand side of Eq. (2) shows the mass accumulation of the component $j$. The first, second, and third terms on the right-hand side of Eq. (2) represent the mass balance due to the diffusion-dispersion process, the advection process, and the geochemical reactions, respectively. The fourth term on the right-hand side of Eq. (2) shows the interphase mass transfer of the component $j$ in $mol/(m^3.s)$. $S_{j_\beta}$ shows the mass transfer of the component $j$ between the phase $\beta$ and an external source in $mol/(m^3.s)$. In this paper, $q_\beta$ is equal to zero because the system is a batch experiment. There is no external source and the system is considered to be a single-phase fluid. Therefore, $\zeta_{j\beta}$ and $S_{j_\beta}$ are equal zero.

$D^*_{j_\beta}$ is a tensor which is a function of the type of the porous medium and the fluid velocity as follows (Benjamin and Lawler, 2013):

$$D^*_{j_\beta} = D_{j_\beta} + \epsilon_{j_\beta} \tag{3}$$

where $D_{j_\beta}$ and $\epsilon_{j_\beta}$ are the effective diffusion and dispersion coefficients of component $j$ in phase $\beta$, respectively. Eq. (3) represents the diffusion model which has been used in modeling. For a porous medium, the value of the effective diffusion coefficient, $D_{j_\beta}$, is between 0.6 and 0.7 of the molecular diffusion coefficient, $D^0_{j_\beta}$, which is measured in the absence of the porous medium (Perkins and Johnston, 1963). The following equation shows the relationship between the molecular diffusion coefficient and the effective diffusion coefficient (Perkins and Johnston, 1963):

$$\frac{D_{j_\beta}}{D^0_{j_\beta}} = \frac{1}{F\phi} \tag{4}$$

where $F$ is the formation electrical resistivity and $\phi$ is the porosity. The value of $F$ is also a function of porosity (Lyons and Plisga, 2011). Thereby, it changes within a porous medium. In this study, based on Archie's Law ($F = \phi^{-m}$, $m$ is the cementation factor) $F$ is equal to 14.26 for a porosity of 0.19 with a cementation factor of 1.6 for the considered cement (Matyka et al., 2008). Although, the diffusion coefficient in Eq. (4) can also be represented in terms of tortuosity as follows (Promentilla et al., 2009):

$$\frac{D_{j_\beta}}{D^0_{j_\beta}} = \frac{1}{\tau} \tag{5}$$

where $\tau$ is the tortuosity. It can be deduced from $F\phi$ that $\tau$ should be equal to 2.70 for a porosity of 0.19. The diffusion coefficient $D_{j\beta}$ of a molecule in a liquid is a function of temperature and viscosity which can be calculated based on the Stokes-Einstein equation as:

$$D_{j\beta} = \frac{kT}{6\pi\mu r} \tag{6}$$

$D$ is the diffusion coefficient of a molecule in liquids, $\mu$ is the solvent viscosity, $T$ is the temperature, $r$ is the radius of the diffusing particle, and $k$ is the Boltzmann constant. This equation is usually considered as a standard to which other methods are compared (Cussler, 1997; Kuhn et al., 2009). $\epsilon_{j_\beta}$ shows the dispersion coefficient of component $j$ in phase $\beta$ which can be calculated as follows:

$$\epsilon_{j_\beta} = \alpha_j q^n_\beta \tag{7}$$

Where, $\alpha_j$ is dispersivity of component $j$, which can be different for the longitudinal and the transverse directions, and $n$ is a constant which depends on the porous media (Delgado, 2007).

The reactions that considerably rapidly progress are thermodynamically controlled; in this case, they can be accounted for based on their equilibrium constants. The slow reactions are kinetically controlled. Indeed, they follow a form of rate law depending on the type of reaction (Steefel et al., 2015; Xu et al., 2004). This assumption simplifies the application of numerical simulations. The reaction rate between the solid and the liquid phase can be characterized using the transition state theory as follows (Aagaard and Helgeson, 1982):

$$R_m = -A_m \sum_{j=1}^{N_{M-L}} k_j a_{H^+}^{(n_{H^+})_j} \left(\Pi a_i^{(n_i)_j}\right)\left(1 - \left(\frac{IAP_j}{K_{eq_j}}\right)^{m_{1_j}}\right)^{m_{2_j}} \tag{8}$$

**Table 1**
The properties of the species involved in the reactions. The accuracy and the associated uncertainty for each value can be found in their corresponding references. For example, the density of calcium carbonate is in the range of 2.7-2.9 gr/cm$^3$ National Center for Biotechnology Information, 2022). Although their value may differ in various literature, it is not significant. Albeit, the difference between them and the values in Table 1 should be negligible. Their effect on the simulation results would not be remarkable in this case. It implies that the predicted trend is almost correct and reliable for cement, with values very close to those in this table. In this paper, their effect on the simulation results is negligible. It implies that the predicted trend is almost correct and reliable. The rate constants and equilibrium constants listed in this table are for the reactions described in Eqs. (9)–((13).

| Property | CH | calcium carbonate | C-S-H(1.6) | $SiO_2$(am) | Ettringite | Inert |
|---|---|---|---|---|---|---|
| Mineral density ($\rho$) in g/cm$^3$ | 2.241 | 2.710 | 2.052 | 2.072 | 1.775 | 3.310(1) |
| Young's modulus (E) in GPa | 38.50(2) | 70.00(3) | 25.55(4) | 159.00(5) | 20.07(6) | 117.60(7) |
| Poisson's ratio ($\nu$)(8) | 0.25 | 0.25 | 0.25 | 0.25 | 0.25 | 0.25 |
| Bulk modulus (K) | 25.67 | 46.67 | 17.03 | 106.00 | 13.38 | 78.40 |
| Shear modulus (G) | 15.40 | 28.00 | 10.22 | 63.60 | 8.03 | 47.04 |
| Specific surface area(9) (SSA) in m$^2$/g | 16.5 | 1.0 | 45.0 | 1.0 | 9.0 | - |
| Log(k [mol/m$^2$.s])(10) | -5.4 | -5.1 | -7.5 | -10.0 | -8.0 | - |
| Log($K_{eq}$) at 25°C(11) | 22.812 | 1.847 | 28.002 | -2.714 | 62.536 | - |
| Initial composition in volume fraction | 0.2000 | 0.0001 | 0.4500 | 0.0199 | 0.0700 | 0.0700 |

(1) The inert solid part is the component that remains intact during reactions and is assumed to be a mixture of the unhydrated clinker; an average value is derived from it (Balonis and Glasser, 2009).
(2) An average value is derived from (Chamrova, 2010; Constantinides and Ulm, 2004).
(3) An average value is derived from Merkel et al. (2009). The value of the Young's modulus will change due to the degradation and the precipitation processes within the pores of calcium carbonate during the invasion of $CO_2$-bearing fluids. For example, a 30% porosity in CC reduces its UCS from 70.00 to 15.00 MPa (please, refer to Eq. (17)).
(4)
(5) An average value is derived from Chamrova (2010), Constantinides and Ulm (2007), Jennings et al. (2007).
(6) The silica gel zone is assumed to be composed of silicon; the average value is derived from (Hopcroft et al. (2010), Moner-Girona et al. (1999).
(7) An average value is derived from Yang and Guo (2014).
(8) It was assumed to be similar to tricalcium silicate (Haecker et al., 2005).
(9) A representative Poisson's ratio is extracted from Chamrova (2010), Constantinides and Ulm (2004), Harsh et al. (1990), Velez et al. (2001), Wang and Subramaniam (2011) and considered equal for the solid components. This value changes in different studies for each solid part of the cement matrix, but an average value can be considered.
(9), (10), and (11) are the geochemical properties extracted from the CrunchFlow database (Steefel et al., 2015). (12), (13), and (14) It should be noted that the values for CSH and ettringite (they were uncertain) were manipulated to obtain a match between the results of the mechanical model and data in Table 4.

where $R_m$ is the rate of the dissolution ($R_m < 0$) or the precipitation ($R_m > 0$) of the mineral component, $m$, in the solid phase in $mol/s$, $A_m$ is the reactive surface of the mineral, in $m^2$, $N_{M-L}$ is the number of the reactions involving the component, $m$, $k_j$ is the rate constant of the reaction, $j$, in $mol/(m^2.s)$, $a_{H^+}$ is the activity of Hydrogen ions, and the term $a_{H^+}^{(n_{H^+})_j}$ is applied to show the rate dependency of reaction, $j$, on the pH, $a_i$ is the activity of the species, $i$, in the liquid phase, $\Pi a_i^{(n_i)_j}$ is applied to consider the catalytic/inhibitory effect of species in the liquid phase on the reaction $j$ (Dávila et al., 2016), $IAP_j$ is the ionic activity product of the reaction, $j$. $K_{eq_j}$ is the equilibrium constant for the reaction, $j$. $K_{eq}$ is also referred to as either the solubility product or the thermodynamic solubility product corresponding to the dissolution or the precipitation of minerals. $m_{1_j}$ and $m_{2j}$ are parameters characterising the dependency of the reaction, $j$, on the saturation index (SI) which is equal to $log(IAP_j/K_{eq_j})$.

In this study, the cement cores are assumed to be fully saturated. The following reactions are extracted from the CrunchFlow (Steefel et al., 2015) database as the reactions occurring within the cement matrix due to the invasion of $CO_2$-bearing fluids ($Ca(OH)_2$, $CSH(1.6)$, $CaCO_3$, $SiO_2(am)$, *Ettringite* are solid species and the remaining are aqueous):

$$Ca(OH)_2 + 2H^+ \leftrightarrow + Ca^{2+} + 2H_2O \quad (9)$$

$$CSH(1.6) + 3.2H^+ \leftrightarrow + 1.6Ca^{2+} + SiO_2(aq) + 2.18H_2O \quad (10)$$

$$CaCO_3 + H^+ \leftrightarrow + HCO_3^- + Ca^{2+} \quad (11)$$

$$SiO_2(am) \leftrightarrow SiO_2(aq) \quad (12)$$

$$Ettringite + 12H^+ \leftrightarrow + 2Al^{3+} + 3SO_4^{2-} + 6Ca^{2+} + 38H_2O \quad (13)$$

Eqs. (9), (10), and (13) show the dissolution of CH, C-S-H, and Ettringite, respectively. The AS gel is shown by $SiO_{2(am)}$, which is in equilibrium with $SiO_{2(aq)}$ in Eq. (12). The mechanical, thermodynamical, and kinetic properties of the solid species are outlined in Table 1.

**Table 2**
Diffusion coefficient (please, refer to either Eqs. (4) or (5)) of the aqueous species in water at 25 °C (Cussler, 1997; Kestin et al., 1981; Li and Gregory, 1974; Rebreanu et al., 2008).

| Species | $D_0$ ($10^{-6}\frac{cm^2}{s}$) |
|---|---|
| $H^+$ | 93.1 |
| $Ca^{2+}$ | 7.93 |
| $OH^-$ | 52.7 |
| $Cl^-$ | 20.3 |
| $HCO_3^-$ | 11.8 |
| $CO_3^{2-}$ | 9.55 |
| $CO_2$(aq) | 19.2 |
| $SiO_2$(aq) | 11.7 |
| $Na^+$ | 13.3 |
| Other species | 10.00 |

In this study, the CrunchFlow code, developed by Steefel et al. (2015), has been used to simulate the geochemical alteration of the cement matrix due to exposure to supercritical $CO_2$. In these simulations, it has been assumed that the outer face of the cement cores is constantly in contact with the supercritical $CO_2$. Therefore, the Dirichlet boundary condition, considering a constant concentration of $CO_2$, is assumed to dominate the cement-fluid interface. The cement matrix is initially assumed to be saturated with brine which only contains dissolved NaCl with a concentration of 0.5 mol/L.

The diffusion coefficients for each of the aqueous phases in Eqs. (9)–(13) can be found in Table 2. The reactions occurring with the aqueous phase are outlined in Table 3.

**Table 3**
Reactions within the aqueous phase with their equilibrium constants at 25 °C extracted from CrunchFlow database (Steefel et al., 2015).

| Aqueous phase reactions | Log ($K_{eq}$) |
|---|---|
| $CO_2(aq) + H_2O \leftrightarrow H^+ + HCO_3^-$ | -6.3447 |
| $CaCl_2(aq) \leftrightarrow Ca^{2+} + 2Cl^-$ | 0.64 |
| $CaOH^+ + H^+ \leftrightarrow H_2O + Ca^{2+}$ | 12.781 |
| $H_2SiO_4^{2-} + 2H^+ \leftrightarrow SiO_2(aq) + 2H_2O$ | 22.9600 |
| $H_4(H_2SiO_4)_4^{4-} + 4H^+ \leftrightarrow 4SiO_2(aq) + 8H_2O$ | 35.9400 |
| $H_6(H_2SiO_4)_4^{2-} + 2H^+ \leftrightarrow 4SiO_2(aq) + 8H_2O$ | 13.6400 |
| $HCl \leftrightarrow H^+ + Cl^-$ | -0.6700 |
| $H_2SiO_3^- + H^+ \leftrightarrow SiO_2(aq) + H_2O$ | 9.9525 |
| $NaCl(aq) \leftrightarrow Na^+ + Cl^-$ | 0.7770 |
| $NaHSiO_3 + H^+ \leftrightarrow SiO_2(aq) + H_2O + Na^+$ | 8.3040 |
| $NaOH \leftrightarrow Na^+ + OH^-$ | 14.7948 |
| $CO_3^{2-} + H^+ \leftrightarrow HCO_3^-$ | 10.3288 |
| $CaCO_3(aq) + H^+ \leftrightarrow Ca^{2+} + HCO_3^-$ | 7.107 |
| $CaHCO_3^+ \leftrightarrow Ca^{2+} + HCO_3^-$ | -1.103 |
| $NaCO_3^-(aq) + H^+ \leftrightarrow Na^+ + HCO_3^-$ | 9.8144 |
| $NaHCO_3(aq) \leftrightarrow Na^+ + HCO_3^-$ | -0.1541 |

### 2.2.2. Mechanical modeling

In this study, the Voigt model (Liu et al., 2009; Zhu et al., 2015) has been applied for calculating Young's modulus of the cement matrix as follows:

$$E_{0,r}^t = \sum_{i=1}^{N_m} E_i f_{i,r}^t \tag{14}$$

where $E_{0,r}^t$ is Young's modulus of the cement matrix with a porosity of zero at the time, $t$, and the radius, $r$, $E_i$ is Young's modulus for the mineral $i$ as shown in Table 1, $f_{i,r}^t$ shows the volume fraction of the mineral $i$ over the entire volume of the solid phase, and $N_m$ is the number of minerals in the cement matrix. The value of $E_{0,r}^t$ is corresponded to the Young's modulus of the cement matrix, $E_r^t$, at the time, t, and the radius, $r$, as follows (Phani and Niyogi, 1987):

$$E_r^t = E_{0_r}^t \left(1 - a\phi_r^t\right)^{n_r^t} \tag{15}$$

where the parameters of $a$ and $n$ are material constants that are functions of the time and the radius. It was assumed that at $\phi = 1$, Young's modulus is zero, which implies that $a$ is considered equal to one (Lafhaj et al., 2006; Li et al., 2006). The value for $n$ is set at 1.65 to fit the numerical Young's modulus with that value for the intact cement matrix. The UCS is calculated using the following equation (Jurowski and Grzeszczyk, 2018):

$$UCS_r^t = k_s(1-\gamma)\left(\frac{10^6 E_r^t}{43\rho^{1.5}}\right) \tag{16}$$

where $k_s$ is a coefficient that depends on the cement type (i.e., referring to the binder type such as CEM I), $\gamma$ shows the volume ratio of aggregates. This value is assumed to be zero based on using plain cement paste for the well-cementing job, $\rho$ is density in kg/m$^3$ and $UCS_r^t$ is the UCS for the cement matrix in MPa at the time, $t$, and the radius, $r$. The value of $k_s$ was found to be 1.18 to match the UCS of the intact cement matrix.

## 3. Results and discussions

### 3.1. Experimental results

The initial porosity before carbonation is 19%; it is low compared with other cement types in the context of geological storage. In general, porosities from MIP tests in the literature are almost twice as high as in this work. For example, Fabbri et al. (2009) obtained a porosity of 41%, Barlet-Gouedard et al. (2007) reported a porosity of 33%, and Urbonas et al. (2016) had porosity values ranging from 37.6 to 44.5%, depending on the water to cement ratio. Nevertheless, these experiments were

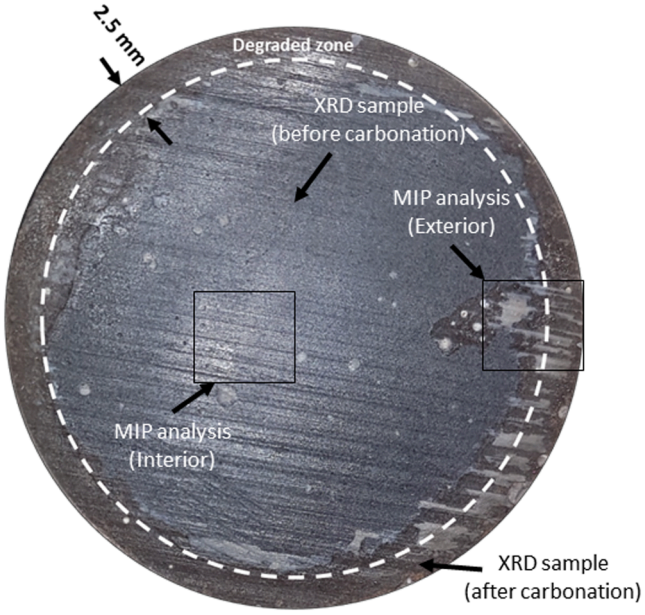


**Fig. 1.** Visible degradation front in specimen carbonated for 30 days at 20 MPa and 90°C.

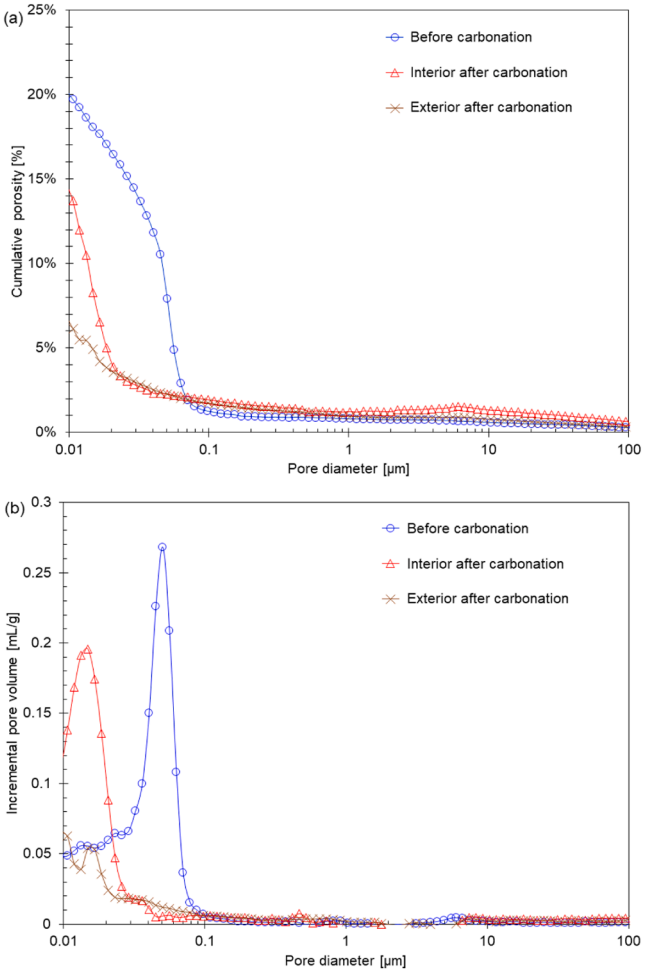


**Fig. 2.** Porosity variation over the exterior, and the interior of the sample after 30 days of carbonation at 20 MPa and 90°C. (a) cumulative porosity, and (b) incremental pore volume.

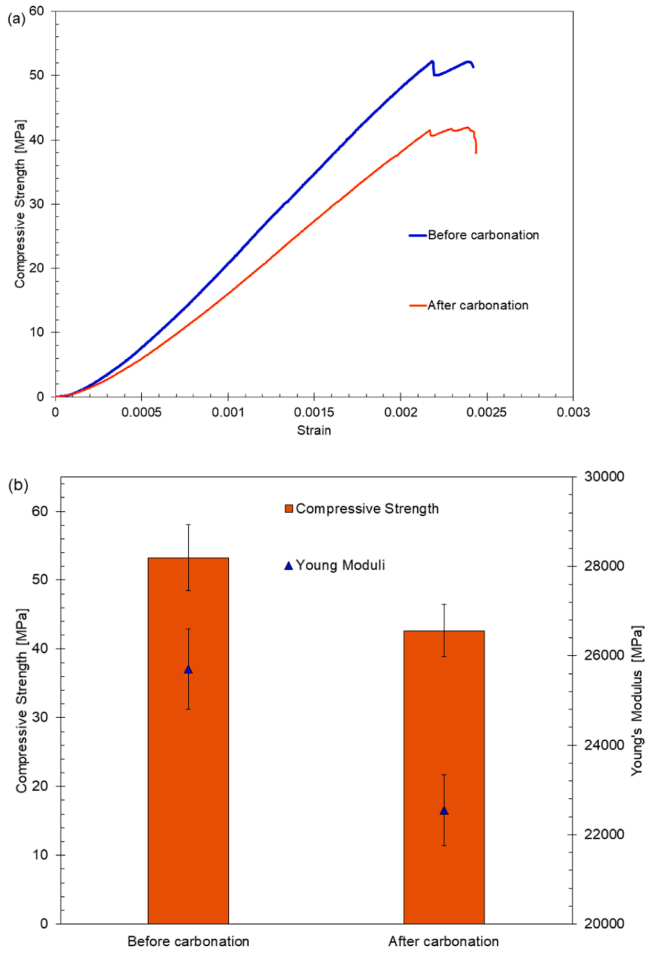


**Fig. 3.** (a) Stress-strain curve during uniaxial compression tests, and (b) specimens' compressive strength and the Young's Modulus variation after 30 days of carbonation at 20 MPa and 90°C. These properties are for a material presenting significant heterogeneities in composition and thus strength. The Young's modulus is equal to the slope of the stress versus strain within the elastic zone. The UCS is assumed as the peak of the stress which the cement can bear before the failure.

performed on samples cured at high temperatures and within a short period. Indeed, porosity decreases with decreasing curing temperature (Bahafid et al., 2017) and extended curing time (Bahafid, 2017).

de Sena Costa et al. (2018) showed that the pH level is reduced over a wider area in specimens tested underwater. The curing conditions allowed water to saturate the cement samples, and $CO_2$ was diffused into the water. The rate of $CO_2$ diffusion into the water depends on the pressure and temperature to which the system is subjected. For porous materials, it also depends on their porosity (Vallin et al., 2013). Fig. 1 shows the advancement of the carbonation front in a cement specimen after 30 days. MIP samples were taken from the most degraded area (Exterior) and the area near the core (Interior). Here, two sections can be distinguished due to the chemical reactions caused by the advance of $CO_2$-bearing fluids from the external boundary. The outer ring section includes precipitated CCs as confirmed in Fig. 5. It can be observed in Fig. 5 that the amount of CC in form of calcite and aragonite increases after carbonation. The inner section is characterized by the dissolution-precipitation effects because the porosity in that section is decreasing, signaling the precipitation of CCs in the interconnected pores. This statement is verified in Fig. 2.

The dissolution-precipitation process during carbonation allows CC to fill the interconnected pore network because the molar volume of CC is higher than that of CH. This effect is shown in Fig. 2, where the porosity in the exterior zone of the sample is reduced to 6%, and in the interior zone, it is reduced to 14%.

A larger quantity of CC will precipitate where the ion concentration is high. However, it also depends on other parameters such as pH. This generates a porosity profile in which the porosity in areas close to the exposed surface is reduced (i.e., within locations deeper than the degraded zone formed on the outer face of the cement matrix). In contrast, the inner parts of the cement core are less affected. Studies carried out by Rimmelé et al. (2008b) and then supported by Cheshire et al. (2017) revealed a macroscale porosity profile suggesting different rates of CC precipitation throughout the cement matrix. In this study, the porosity results in the interior parts of the cement matrix reveal that it has been less prone to CC precipitation, showing a porosity of 14%. Another porosity profile can also be observed on microscale in the work of Kutchko et al. (2007). Their experiment showed the formation of different zones. The porosity within the most inner parts slightly increased. Due to CC precipitation, the porosity decreased in the next zone towards the outer face. They observed that the porosity within the outermost layer significantly increased due to the considerable depletion of calcium. Nevertheless, the porosity of different zones observed in the latter work was estimated by analyzing the scanning electron microscope images. Therefore, it cannot be reliably quantified, and the area under consideration is very small.

These decreases in porosity produce a clogging effect opposing the incoming $CO_2$ flow. Furthermore, Bagheri et al. (2018) suggest that the permeability will reduce if the flow's direction is parallel to the diffusion and increase if the flow is perpendicular to the diffusion (Xu et al., 2019; Yuanhua et al., 2013). This effect was seen by Barría et al. (2022), where the carbonation degree follows a logarithmic trend, implying that the reaction advance slows down over time.

Morandeau et al. (2015, 2014) mentioned that most of the variation in porosity during the carbonation process is due to the carbonation of the C-S-H phase. This means that the drop in porosity in the samples in this study is mainly due to C-S-H decalcification. As C-S-H is the main contributor to the mechanical strength, its behavior is considerably changed. Fig. 3 shows a decrease in the mechanical properties of Class G cement. Indeed, the overall porosity alteration and the dissolution-precipitation of the material's composing phases induce a variation in the apparent mechanical properties of the cementitious material (Bagheri et al., 2019).

Atmospheric carbonation on cement increases its compressive strength (Ashraf, 2016). This is induced by the simultaneous leaching of calcium from CH and C-S-H. One mol of CH is replaced by one mol of CC, and as the mechanical properties of CC are higher than CH, a strength increase is expected. On the other hand, as the C-S-H molecular structure is not defined and depends on several factors during the hydration process, natural carbonation may decalcify C-S-H on a minor scale, where no decrease in strength is expected. Under extreme conditions, the compressive strength is affected due to the higher degradation of C-S-H resulting from breaking its chains and filling the pores with CC. Even though CC may have stronger properties, it will not be bounded to the cement matrix as the former C-S-H was bounded at a nanoscale. Once CH is depleted, the C-S-H decalcification allows a higher production of CC. Thus, the considerable porosity reduction seen in the results here is a consequence of a large amount of C-S-H being degraded and also the dissolution of CH, allowing the mechanical strength to decrease during carbonation. Therefore, although the porosity decreases, the UCS shows a reduction for three reasons: (1) the CSH is degraded, (2) the precipitated CC does not fill the pores to bear the stress i.e., they are precipitated on the surface of the pores and practically have no positive impact on UCS, (3) the CC has not a strong from due to the intrinsic porosity occurring within itself during the precipitation.

Furthermore, during the compressive strength tests, a small layer of material was observed to be the first part to be dislodged in different sectors of the sample when a small force was applied, suggesting that there is a thin layer on the external surface of the specimen subjected to


**Fig. 4.** Cement specimen after carbonation for 30 days at 20 MPa and 90°C.

$CO_2$-bearing fluids that has a very low mechanical strength. This layer was also seen by Kutchko et al. (2007), Jeong et al. (2018), and Rimmelé et al. (2008b). In this layer, the bicarbonation process begins, where the solid CC phase is dissolved and forms $HCO_3^-$ ions. This process increases the porosity of this layer and leaves it with lower mechanical resistance. In some samples, it was possible to see a very thin layer of material that could be removed by scratching the cement surface (Fig. 4). As shown in Fig. 4, a thin layer from the surface of the most degraded samples can be removed by scratching the surface, indicating high porosity and low bonding of the material to the core. The re-dissolution of CC on the surface of the cement reduces the amount of material contributing to the resistance, which explains the overall decrease in its mechanical performance. Fig. 5 shows the XRD pattern for a non-carbonated specimen and a carbonated specimen near the outer face of the cement matrix. In non-carbonated cement, the crystalline phase shows a strong reflection of Portlandite. Aluminates such as Katoite are also observed. The presence of calcium carbonates in the specimen indicates that a certain percentage of carbonation has occurred due to exposure to $CO_2$. In the specimen, smaller percentages of Brownmillerite are also detected. Carbonated cement contains 85% calcium carbonates, of which 73% are aragonite and 12% calcite. There is only 5% Portlandite, and 9% Brownmillerite. The latter is the last part which is affected, because portlandite is the first mineral in the cement matrix which is carbonated and after that C-S-H is also affected. The non-hydrated cement products are surrounded by this C-S-H layer (Shah et al., 2018), which protects it until all the C-S-H is carbonated.

Fig. 2 shows that the precipitation of CCs due to the invasion of carbon species into the cement pores results in shifting PSD towards lower values. The probability of increasing the gel pores is low because they do not participate in the flow. Thereby, they do not contribute to the porosity alteration. The dissolution of Portlandite contributes to an increase in the capillary porosity, although the precipitation of CC easily compensates it. Indeed, with the precipitation of CC, the size of capillary pores is reduced. Therefore, the main mode of the PSD also shifts towards lower porosity values. It can be understood from Fig. 2 (a) and Table 4 that the value of porosity for the carbonated zone decreased from 19% to 6%. The peak strength and Young's modulus decrease for the whole cement matrix, as can be observed in Fig. 3 (a) and (b). This observation appears to be contradictory when the precipitation of the CC is also accounted for in this study. The literature, such as (Lecampion et al., 2011; Walsh et al., 2014), showed that the precipitation of CC leads to an increase in the cement strength. It could be the result of the short period of hydration. In their work, the hydration process of the cement matrix probably continued to a great extent even after exposure to $CO_2$-bearing fluids, which helps the cement strength. In this work, the

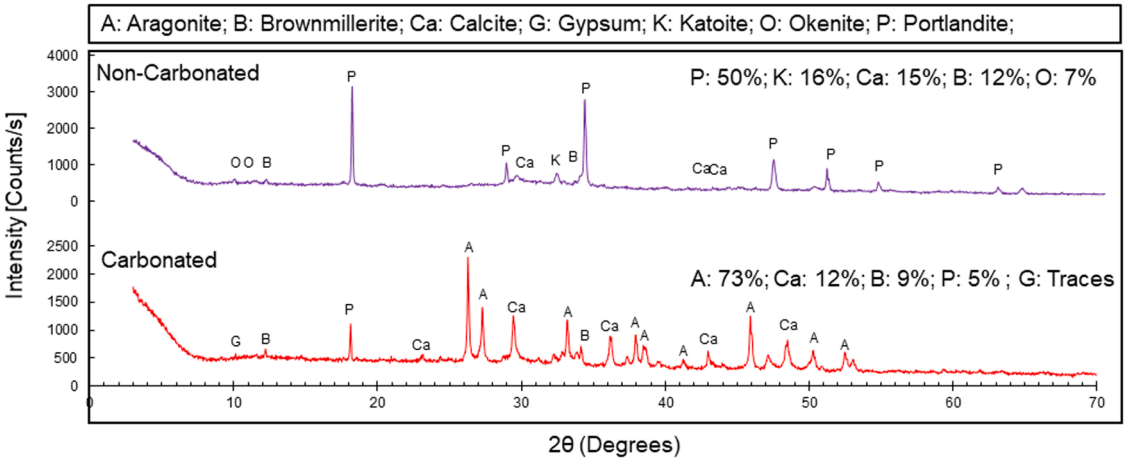


**Fig. 5.** XRD pattern results before carbonation and at the outer rim after 30 days of carbonation. The data in this figure are calibrated to account for porosity and CSH to be used in calculations in this paper.

**Table 4**
The change in density, the uniaxial compressive strength (UCS), Young's modulus (E), and porosity prior to and after exposure to supercritical $CO_2$. For the carbonated cement, all parameters are reported for the whole cement matrix except for the porosity which is attributed to the carbonated zone within the cement matrix.

| | Non-carbonated cement | | | | Carbonated cement | | | | | |
|---|---|---|---|---|---|---|---|---|---|---|
| | $\rho\ (\frac{gr}{cm^3})$ | UCS (MPa) | E (GPa) | Porosity (%) | $\rho\ (\frac{gr}{cm^3})$ | Mass uptake (gr) | UCS (MPa) | E (GPa) | Penetration depth (mm) | Porosity (%) |
| Result | 1.99 | 53.26 | 25.70 | 19 | 2.02 | 2.7 | 42.66 | 22.55 | 2.5 | 6 |
| Variation (±) | 0.01 | 4.8 | 1 | 0.7 | 0.02 | 1.2 | 5.64 | 0.85 | 1.4 | 1.5 |

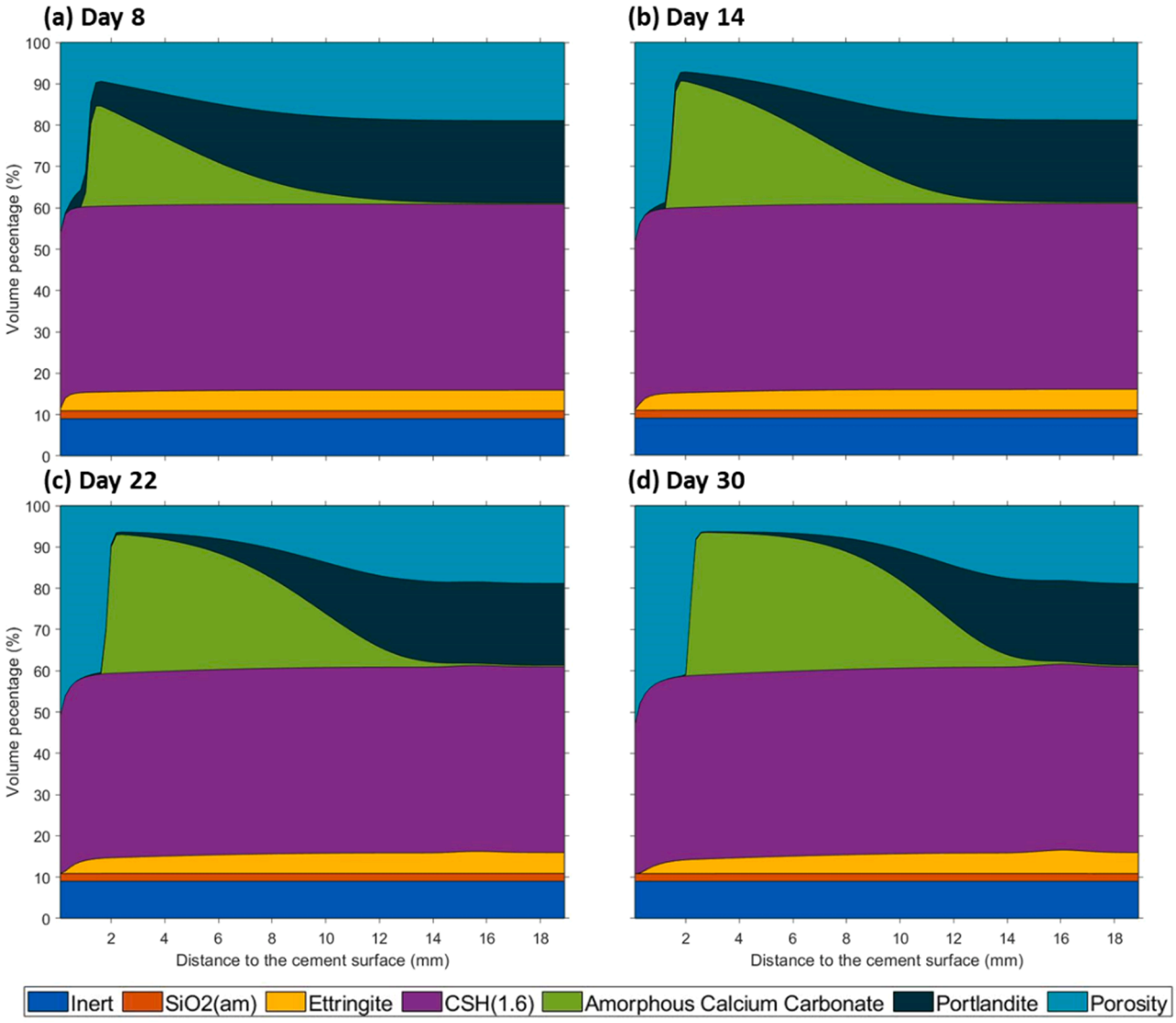


**Fig. 6.** The profiles for the mineral contribution at (a) day 8, (b) day 14, (c) day 22, (d) day 30 after exposure to supercritical $CO_2$ predicted by numerical modeling. The initial composition is reported in Table 1. C-S-H can be decalcified and becomes porous. However, in this study those pores do not contribute to the flow. It implies that its volume fraction can remain almost constant.

cement matrices cured near to completeness. It was observed that the Uniaxial Compressive Strength (UCS) and Young's modulus decrease during the ongoing carbonation process in the pores of the cement matrix.

The studies (Baird et al., 1975; Black et al., 2008, 2007; Brečević and Nielsen, 1989; Cole and Kroone, 1960; García-González et al., 2007; Moorehead, 1986; Morandeau et al., 2014; Shah et al., 2018) have shown that the precipitation of CC will be in an amorphous or a weak crystalline form, particularly once it precipitates. The early amorphous or weak crystalline CC will progressively be converted to calcium carbonate. In this study, it is perceived that CC has a weak form. Therefore, despite the precipitation of CC and a decrease in the porosity, the precipitation of CC does not practically contribute to the cement strength. The mechanical properties of the cement matrix are a function of the cement composition (Liu et al., 2009; Zhu et al., 2015), which evolves during the carbonation process.

### 3.2. Numerical modelling

Fig. 6 (a)–(c) shows the gradual emergence of the amorphous CC from day 8 to day 30 after exposure to supercritical $CO_2$. In Fig. 6 (c), it can be seen that the peak of CC precipitation is at the depth of 2.4 mm and the value for the porosity is around 6% which shows a good match to the reported values in Table 4 for the penetration depth and porosity, respectively. The UCS of the cement matrix is a result of the combined effect of the different contributing minerals. Their evolution directly affects the average UCS. Generally, it is expected that UCS should increase within the CC precipitation zones and shows a decrease for areas near the outer face. In Fig. 8, the UCS and Young's modulus changes are simulated. Fig. 8 demonstrates that the cement matrix degrades at less than 2.4 mm depths. It implies that the values for its mechanical properties significantly reduce near the cement-supercritical $CO_2$ interface. CH is wholly depleted in this region, and C-S-H also experiences calcium leaching, as shown in Fig. 6. This zone is referred to as the silica gel zone (or degraded zone). CC starts occupying the pores at depths from 2.4 to 14.0 mm but is not strong enough to improve the UCS. Therefore, despite normal expectations, the value of UCS and Young's modulus shows a decrease in the CC precipitation zone. It can be understood from Fig. 6 that the CH dissolution starts from depths around 14 mm and is accelerated approaching the cement outer face.

As shown in Fig. 6, the inert part and $SiO_2$ are not affected by the attacking supercritical $CO_2$. It should be noted that supercritical $CO_2$

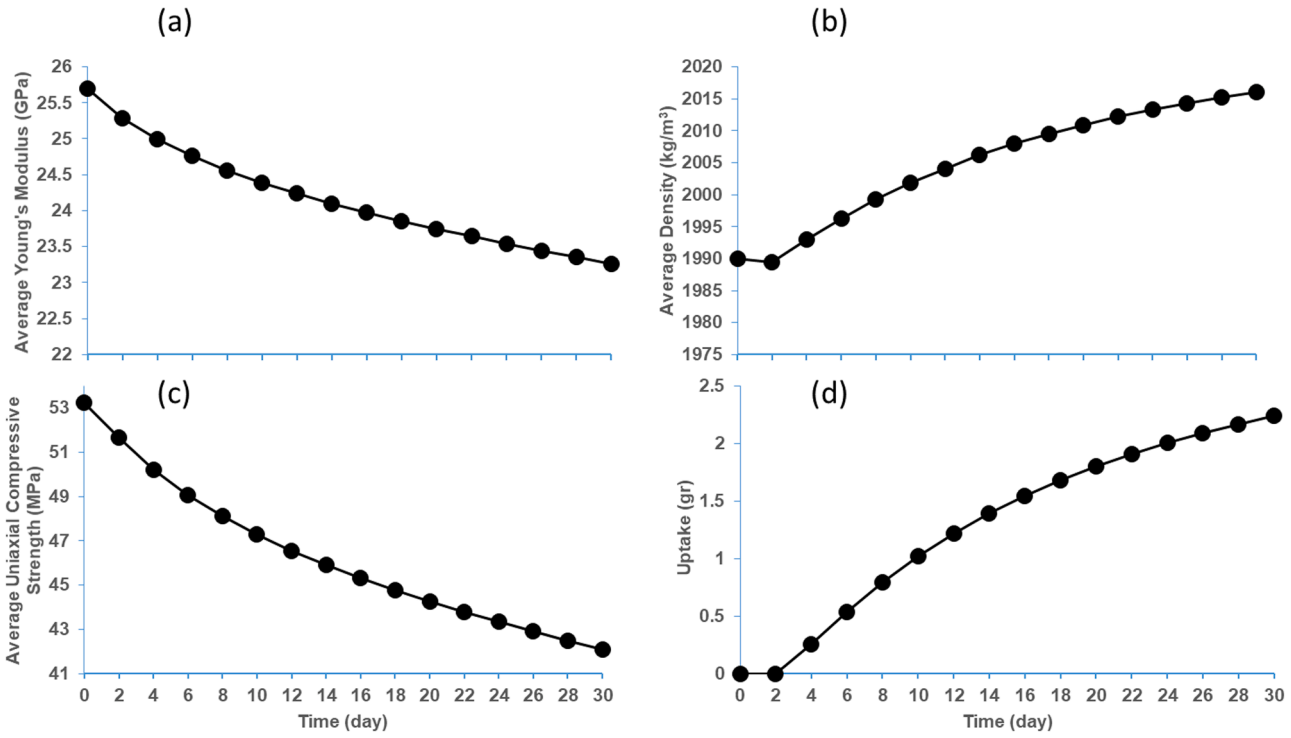


**Fig. 7.** Change in the properties of the cement matrix during 30-day period obtained from numerical modeling, (a) the average Young's modulus (MPa), (b) the average density (kg/m$^3$), (c) the average uniaxial compressive strength, (d) the mass uptake (g).

needs to be dissolved in brine to react with the solid phase. At the outer face of the cement matrix, $CO_2$ dissolves in brine and then starts diffusing into the inner parts of the cement matrix. It can be observed in Fig. 6 that the CC zone gradually extends into the inner parts of the cement matrix.

The change in the average properties of the cement matrix is predicted using numerical modeling and shown in Fig. 7. It can be seen in Fig. 7(a) and (c) that at day 30 the average value of UCS reduces to 45.10 MPa and Young's modulus approaches 23.25 GPa. The average value for Young's modulus is a linear weighted average of the radial sections in a cylindrical core. The weighing factors equal the ratio of those radial areas to the whole cylindrical area. Then, the value for UCS is computed using Eq. (16). The average density equals the overall mass over the volume in which mass is changing due to chemical reactions. UCS and Young's modulus values are close to the values reported in Table 4. The mass uptake and density magnitudes are 2.24 g and 2.0160 g/cm$^3$ at day 30 in Fig. 7(d) and (b), which are comparable to the values measured in the experiments as shown in Table 4. It should be noted that Young's modulus for CC in calculations is changed to account for the effect of the intrinsic porosity. The Young's modulus of CC, $E_{cc}$, is 70 GPa, as shown in Table 1. As calcium carbonate is also a mineral, the authors assume that it also follows an equation similar to Eq. (15). It is worth noting that this equation is developed for rocks (Lafhaj et al., 2006; Li et al., 2006). This assumption helps to find a correlation between the porosity and Young's modulus for CC with non-zero porosity. However, the authors believe that the form of this equation is not that vital. Indeed, the crucial feature is that the suggested equation should be able to simulate the decreasing trend. The numerical calculations in this study show that CC should have an amorphous form, as the XRD results indicate. It was understood that Young's modulus could be characterized as follows:

$$\boldsymbol{E}_{a\_cc} = \boldsymbol{E}_{cc}(1-\phi_i)^{n_{cc}}, \tag{17}$$

where $E_{a\_cc}$ is Young's modulus for the amorphous CC, $\phi_i$ is the intrinsic porosity of the amorphous CC, and $n_{cc}$ is an adjusting power constant which is found to be 4.3 in this study. The value of $E_{a\_cc}$ was used in Eq. (14) instead of $E_{cc}$. The value of porosity changes due to the geochemical reactions occurring within the cement matrix. Thereby, its value changes with location. The intrinsic porosity of the amorphous CC does not participate in the flow and can be considered pores similar to the gel pores. This porosity is the main reason that the strengthening effect of the CC precipitation is compromised. The intrinsic porosity of the calcium carbonate increases its overall volume. Thereby, the capillary pores become smaller, as depicted in Fig. 2.

## 4. Conclusion

In this study, the evolution in the properties of Class G oil well cement in contact with supercritical $CO_2$ has been studied. The cement specimens were cured under lime-saturated water for 28 days at a temperature of 20 $^{\circ}C$ and under atmospheric pressure to ensure the highest degree of hydration. This was designed to limit the effect of incomplete hydration on the results. Afterwards, the cement specimens were placed in high pressure and high-temperature vessel at a temperature of 90 $^{\circ}C$ and under a pressure of 90 MPa for 30 days. The change in the properties of the cement matrix was measured. The results showed that the UCS and Young's modulus of the cement matrix were reduced, although CC precipitation was observed in the cement matrix. However, these observations appear to be contradictory. The authors believe that this is due to the intrinsic amorphous property of the precipitated CC and due to the high degradation of C-S-H. Although this precipitation reduces the size of pore throats, it is not strong enough to improve the mechanical properties of the cement matrix. This assumption was tested using numerical modeling. The numerical results reasonably match the experimental data. The numerical results in this study confirm the formation of four main zones in the cement matrix due to exposure to supercritical $CO_2$, namely a silica gel zone (or degraded zone), a CC precipitation zone, a Portlandite dissolution zone, and an intact zone. The associated uncertainty for each parameter in Table 1 (or at least the range in which a parameter could change) is not defined clearly in the literature and needs a comprehensive investigation. A sensitivity study will be required based on the associated uncertainties, although it is

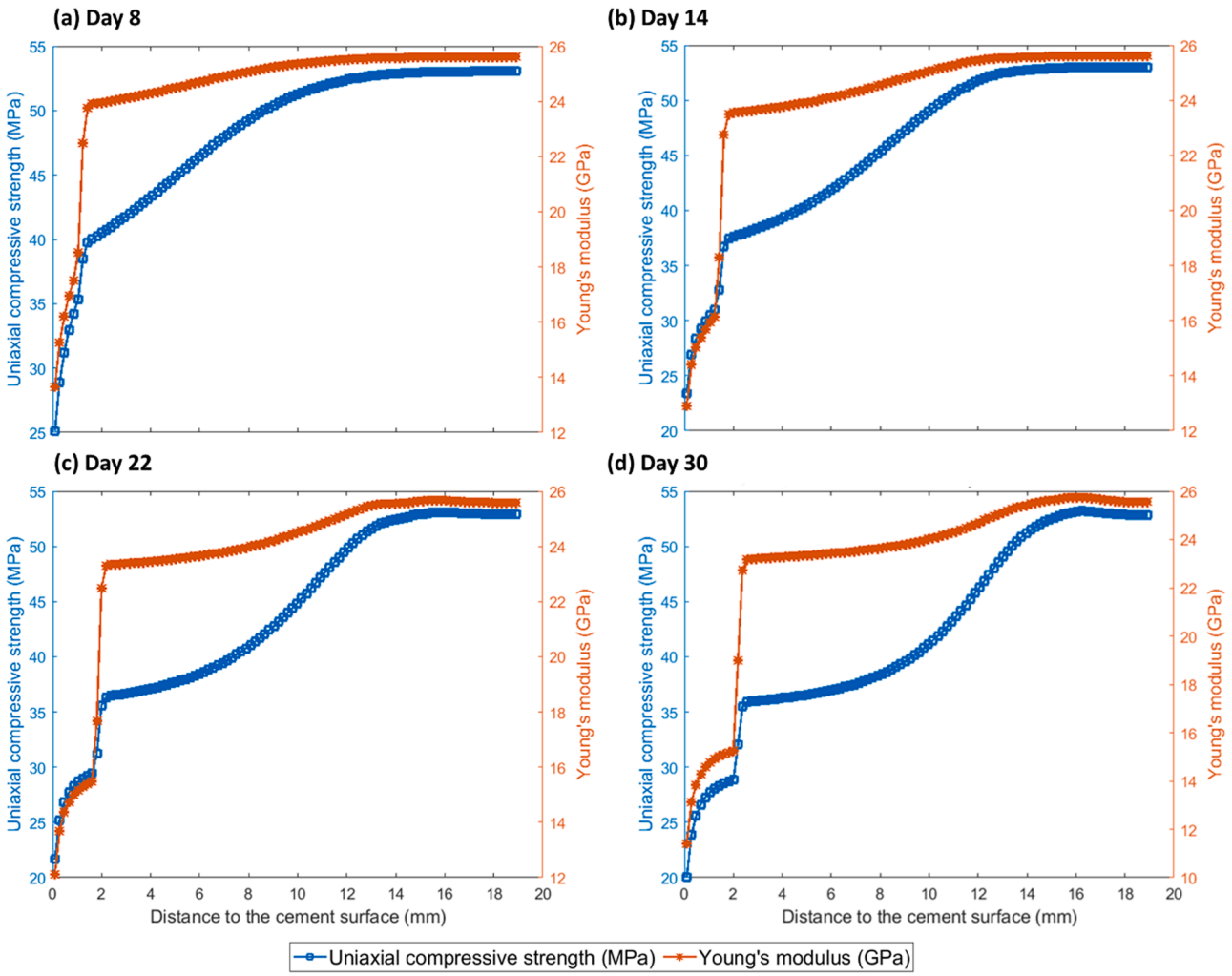


**Fig. 8.** Change in the mechanical properties of the cement matrix, including the uniaxial compressive strength (UCS), and the Young's modulus (E) at (a) day 8, (b) day 14, (c) day 22, (d) day 30 after exposure to supercritical $CO_2$ predicted by numerical modeling.

subject to further studies and reckoned beyond the scope of this paper.

## CRediT authorship contribution statement

**Juan Cruz Barría:** Investigation, Testing, Formal analysis, Data Curation, Visualization, Writing - original draft. **Mohammadreza Bagheri:** Investigation, Software, Validation, Formal analysis, Data Curation, Visualization, Writing - original draft. **Diego Manzanal,:** Conceptualization, Methodology, Writing - review & editing, Supervision, Project administration, Funding acquisition. **Seyed M. Shariatipour:** Conceptualization, Methodology, Writing - review & editing, Supervision, Project administration. **Jean Michel Pereira:** Conceptualization, Methodology, Writing - review & editing, Supervision, Funding acquisition.

## Declaration of Competing Interest

We wish to confirm that there are no known conflicts of interest associated with this publication and there has been no significant financial support for this work that could have influenced its outcome.

## Acknowledgements

The first author gratefully acknowledges the fellowship granted by the National Scientific and Technical Research Council of Argentina (CONICET) and the EIFFEL fellowship program of Excellence granted by the Ministère de l'Europe et des Affaires étrangères of France. The authors acknowledged the financial support of the European Union's Horizon 2020 research and innovation program under Grant Agreement No 101007851 (H2020 MSCA-RISE 2020 Project DISCO2-STORE), the Universidad Nacional de la Patagonia San Juan Bosco -Project UNPSJB PI1614 80020190200006 IP, Res. R/9N°207-2020 CRD1365 FI004/ 17-, the Agency of Scientific and Technological Promotion from the Argentine Republic. (Projects PICT 2016–4543, PICT 2020-SERIEA 02088), and the PIP project N° 11220200103043CO (CONICET). The authors also thank the technical staff of Petroquímica Comodoro Rivadavia and Laboratoire Navier for helping with the tests performed.

## References

Aagaard, P., Helgeson, H.C., 1982. Thermodynamic and kinetic constraints on reaction rates among minerals and aqueous solutions; I, theoretical considerations. Am. J. Sci. 282, 237–285. https://doi.org/10.2475/ajs.282.3.237.

Ajayi, T., Gupta, I., 2019. A review of reactive transport modeling in wellbore integrity problems. J. Pet. Sci. Eng. 175, 785–803. https://doi.org/10.1016/j.petrol.2018.12.079.

API Specification 10A, 2019. Specification for Cements and Materials for Well Cementing, Twenty-Fif. ed. American Petroleum Institute, Northwest Washington, DC.

Asahara, Y., Mito, S., Xue, Z., Yamashita, Y., Miyashiro, K., 2013. Chemical impacts of $CO_2$ flooding on well composite samples: experimental assessment of well integrity for $CO_2$ sequestration. Energy Procedia 37, 5738–5745. https://doi.org/10.1016/j.egypro.2013.06.496.

Ashraf, W., 2016. Carbonation of cement-based materials: challenges and opportunities. Constr. Build. Mater. 120, 558–570. https://doi.org/10.1016/j.conbuildmat.2016.05.080.

Auroy, M., Poyet, S., Le, P., Torrenti, J., Charpentier, T., Moskura, M., Bourbon, X., 2015. Cement and Concrete Research Impact of carbonation on unsaturated water transport properties of cement-based materials. Cem. Concr. Res. 74, 44–58. https://doi.org/10.1016/j.cemconres.2015.04.002.

Bachu, S., Bennion, D.B., 2009. Experimental assessment of brine and/or $CO_2$ leakage through well cements at reservoir conditions. Int. J. Greenh. Gas Control 3, 494–501. https://doi.org/10.1016/j.ijggc.2008.11.002.

Bagheri, M., Shariatipour, S.M., Ganjian, E., 2019. Prediction of the lifespan of cement at a specific depth based on the coupling of geomechanical and geochemical processes for $CO_2$ storage. Int. J. Greenh. Gas Control 86, 43–65. https://doi.org/10.1016/j.ijggc.2019.04.016.

Bagheri, M., Shariatipour, S.M., Ganjian, E., 2018. A review of oil well cement alteration in $CO_2$-rich environments. Constr. Build. Mater. 186, 946–968. https://doi.org/10.1016/j.conbuildmat.2018.07.250.

Bahafid, S., 2017. A multi-technique investigation of the effect of hydration temperature on the microstructure and mechanical properties of cement paste.

Bahafid, S., Ghabezloo, S., Duc, M., Faure, P., Sulem, J., 2017. Effect of the hydration temperature on the microstructure of Class G cement: C-S-H composition and density. Cem. Concr. Res. 95, 270–281. https://doi.org/10.1016/j.cemconres.2017.02.008.

Baird, T., Cairns-Smith, A.G., Snell, D.S., 1975. Morphology and $CO_2$ uptake in tobermorite gel. J. Colloid Interface Sci. 50, 387–391. https://doi.org/10.1016/0021-9797(75)90243-X.

Balonis, M., Glasser, F.P., 2009. The density of cement phases. Cem. Concr. Res. 39, 733–739. https://doi.org/10.1016/j.cemconres.2009.06.005.

Barlet-Gouedard, V., Rimmelé, G., Goffé, B., Porcherie, O., 2007. Well technologies for $CO_2$ geological storage : $CO_2$ -resistant cement. SPE Int. 62, 325–334. https://doi.org/10.2516/ogst.

Barlet-Gouédard, V., Rimmelé, G., Goffé, B., Porcherie, O., 2007. Well technologies for $CO_2$ geological storage: $CO_2$ -resistant cement. Oil Gas Sci. Technol. Rev. l'IFP 62, 325–334. https://doi.org/10.2516/ogst:2007027.

Barría, J.C., Manzanal, D., Pereira, J.M., 2022. Effect of supercritical carbonation on porous structure and mechanical strength of cementitious materials modified with bacterial nanocellulose. Mater. Struct. (Summited to Journal).

Barría, J.C., Vázquez, A., Pereira, J.M., Manzanal, D., 2021b. Effect of bacterial nanocellulose on the fresh and hardened states of oil well cement. J. Pet. Sci. Eng. 199 https://doi.org/10.1016/j.petrol.2020.108259.

Barría, J.C., Manzanal, D., Cerrutti, P., Pereira, J.M., 2021a. Cement with bacterial nanocellulose cured at high temperature: mechanical performance in the context of CO2 geological storage. Geomechanics for Energy and the Environment. https://doi.org/10.1016/j.gete.2021.100267.

Barría, J.C., Manzanal, D., Pereira, J.M., Ghabezloo, 2020. CO2 Geological storage: Microstructure and mechanical behaviour of cement modified with biopolymers after carbonation. E3S Web Conf. Vol. 205, 2020. 2nd International Conference on Energy Geotechnics (ICEGT 2020), section: CO2 Sequestration and Deep Geothermal Energy 18 November 2020. https://doi.org/10.1051/e3sconf/202020502007.

Benjamin, M.M., Lawler, D.F., 2013. Water quality engineering : physical/chemical treatment processes. John Wiley & Sons.

Black, L., Breen, C., Yarwood, J., Garbev, K., Stemmermann, P., Gasharova, B., 2007. Structural features of C-S-H(I) and its carbonation in air-A Raman spectroscopic study. Part II: carbonated phases. Journal of the American Ceramic Society. John Wiley & Sons, Ltd, pp. 908–917.

Black, L., Garbev, K., Gee, I., 2008. Surface carbonation of synthetic C-S-H samples: a comparison between fresh and aged C-S-H using X-ray photoelectron spectroscopy. Cem. Concr. Res. 38, 745–750. https://doi.org/10.1016/j.cemconres.2008.02.003.

Brečević, L., Nielsen, A.E., 1989. Solubility of amorphous calcium carbonate. J. Cryst. Growth 98, 504–510. https://doi.org/10.1016/0022-0248(89)90168-1.

Brunet, J.P.L., Li, L., Karpyn, Z.T., Huerta, N.J., 2016. Fracture opening or self-sealing: critical residence time as a unifying parameter for cement-$CO_2$-brine interactions. Int. J. Greenh. Gas Control 47, 25–37. https://doi.org/10.1016/j.ijggc.2016.01.024.

Brunet, J.P.L., Li, L., Karpyn, Z.T., Kutchko, B.G., Strazisar, B., Bromhal, G., 2013. Dynamic evolution of cement composition and transport properties under conditions relevant to geological carbon sequestration. Energy Fuels 27, 4208–4220. https://doi.org/10.1021/ef302023v.

Cao, P., Karpyn, Z.T., Li, L., 2013. Dynamic alterations in wellbore cement integrity due to geochemical reactions in $CO_2$-rich environments. Water Resour. Res. 49, 4465–4475. https://doi.org/10.1002/wrcr.20340.

Carey, J.W., 2013. Geochemistry of wellbore integrity in $CO_2$ sequestration: Portland cement-steel-brine-$CO_2$ interactions. Rev. Mineral. Geochem. 77, 505–539. https://doi.org/10.2138/rmg.2013.77.15.

Carey, J.W., Svec, R., Grigg, R., Zhang, J., Crow, W., 2010. Experimental investigation of wellbore integrity and $CO_2$-brine flow along the casing-cement microannulus. Int. J. Greenh. Gas Control 4, 272–282. https://doi.org/10.1016/j.ijggc.2009.09.018.

Chamrova, R., 2010. Modelling and Measurement of Elastic Properties of Hydrating Cement Paste.

Cheshire, M.C., Stack, A.G., Carey, J.W., Anovitz, L.M., Prisk, T.R., Ilavsky, J., 2017. Wellbore cement porosity evolution in response to mineral alteration during $CO_2$ flooding. Environ. Sci. Technol. 51, 692–698. https://doi.org/10.1021/acs.est.6b03290.

Choi, B.Y., Lee, H., Chae, G.T., Kim, T., Kim, J.C., 2016. Alteration processes of cement induced by $CO_2$-saturated water and its effect on physical properties: experimental and geochemical modeling study. Chem. Erde Geochem. 76, 597–604. https://doi.org/10.1016/j.chemer.2016.10.001.

Cole, W.F., Kroone, B., 1960. Carbon dioxide in hydrated Portland cement. ACI J. Proc. 56, 1275–1296. https://doi.org/10.14359/8141.

Constantinides, G., Ulm, F.J., 2007. The nanogranular nature of C-S-H. J. Mech. Phys. Solids 55, 64–90. https://doi.org/10.1016/j.jmps.2006.06.003.

Constantinides, G., Ulm, F.J., 2004. The effect of two types of C-S-H on the elasticity of cement-based materials: results from nanoindentation and micromechanical modeling. Cem. Concr. Res. 34, 67–80. https://doi.org/10.1016/S0008-8846(03)00230-8.

Corvisier, J., Brunet, F., Fabbri, A., Bernard, S., Findling, N., Rimmelé, G., Barlet-Gouédard, V., Beyssac, O., Goffé, B., 2010. Raman mapping and numerical simulation of calcium carbonates distribution in experimentally carbonated Portland-cement cores. Eur. J. Mineral. 22, 63–74. https://doi.org/10.1127/0935-1221/2010/0022-1977.

Corvisier, J., Fabbri, A., Brunet, F., Leroy, Y., Goffé, B., Rimmelé, G., Barlet-Gouédard, V., 2013. A numerical model for $CO_2$ wells ageing through water/supercritical $CO_2$/cement interactions. Thermo-Hydromechanical and Chemical Coupling in Geomaterials and Applications. John Wiley & Sons, Inc., Hoboken, NJ, USA, pp. 75–84.

Coussy, O., Ulm, F.-J., 1996. Creep and plasticity due to chemo-mechanical couplings. Arch. Appl. Mech. 66, 523–535. https://doi.org/10.1007/BF00808142.

Cussler, E.L., 1997. Diffusion : Mass Transfer in Fluid Systems. Cambridge University Press.

Dávila, G., Luquot, L., Soler, J.M., Cama, J., 2016. 2D reactive transport modeling of the interaction between a marl and a $CO_2$-rich sulfate solution under supercritical $CO_2$ conditions. Int. J. Greenh. Gas Control 54, 145–159. https://doi.org/10.1016/j.ijggc.2016.08.033.

de Sena Costa, B.L., de Oliveira Freitas, J.C., Silva Santos, P.H., Gomes da Silva Araújo, R., dos Santos Oliveira, J.F., de Araújo Melo, D.M., 2018. Study of carbonation in a class G Portland cement matrix at supercritical and saturated environments. Constr. Build. Mater. 180, 308–319. https://doi.org/10.1016/j.conbuildmat.2018.05.287.

Delgado, J.M.P.Q., 2007. Longitudinal and transverse dispersion in porous media. Chem. Eng. Res. Des. 85, 1245–1252. https://doi.org/10.1205/CHERD07017.

Duan, Z., Sun, R., 2003. An improved model calculating $CO_2$ solubility in pure water and aqueous NaCl solutions from 273 to 533 K and from 0 to 2000 bar. Chem. Geol. 193, 257–271. https://doi.org/10.1016/S0009-2541(02)00263-2.

Duguid, A., Radonjic, M., Scherer, G.W., 2005. Degradation of Well Cements Exposed to Carbonated Brine. Fourth Annual Conference on Carbon Capture and Sequestration 1–12.

Duguid, A., Scherer, G.W., 2010. Degradation of oilwell cement due to exposure to carbonated brine. Int. J. Greenh. Gas Control 4, 546–560. https://doi.org/10.1016/j.ijggc.2009.11.001.

Fabbri, A., Corvisier, J., Schubnel, A., Brunet, F., Goffé, B., Rimmele, G., Barlet-Gouédard, V., 2009. Effect of carbonation on the hydro-mechanical properties of Portland cements. Cem. Concr. Res. 39, 1156–1163. https://doi.org/10.1016/j.cemconres.2009.07.028.

Fernández Bertos, M., Simons, S.J.R., Hills, C.D., Carey, P.J., 2004. A review of accelerated carbonation technology in the treatment of cement-based materials and sequestration of $CO_2$. J. Hazard. Mater. 112, 193–205. https://doi.org/10.1016/j.jhazmat.2004.04.019.

García-González, C.A., Hidalgo, A., Fraile, J., López-Periago, A.M., Andrade, C., Domingo, C., 2007. Porosity and water permeability study of supercritically carbonated cement pastes involving mineral additions. Ind. Eng. Chem. Res. 46, 2488–2496. https://doi.org/10.1021/ie061571o.

Gasda, S.E., Bachu, S., Celia, M.A., 2004. Spatial characterization of the location of potentially leaky wells penetrating a deep saline aquifer in a mature sedimentary basin. Environ. Geol. 46, 707–720. https://doi.org/10.1007/s00254-004-1073-5.

Glasser, F.P., Matschei, T., 2007. Interactions between Portland cement and carbon dioxide. ICCC Conference.

Haecker, C.J., Garboczi, E.J., Bullard, J.W., Bohn, R.B., Sun, Z., Shah, S.P., Voigt, T., 2005. Modeling the linear elastic properties of Portland cement paste. Cem. Concr. Res. 35, 1948–1960. https://doi.org/10.1016/j.cemconres.2005.05.001.

Harsh, S., Shen, Z., Darwin, D., 1990. Strain-rate sensitive behavior of cement paste and mortar in compression. ACI Mater. J. 87, 508–516. https://doi.org/10.14359/1931.

Hopcroft, M.A., Nix, W.D., Kenny, T.W., 2010. What is the Young's modulus of silicon? J. Microelectromechan. Syst. 19 https://doi.org/10.1109/JMEMS.2009.2039697.

Huerta, N.J., Hesse, M.A., Bryant, S.L., Strazisar, B.R., Lopano, C., 2016. Reactive transport of $CO_2$-saturated water in a cement fracture: application to wellbore leakage during geologic $CO_2$ storage. Int. J. Greenh. Gas Control 44, 276–289. https://doi.org/10.1016/j.ijggc.2015.02.006.

Huet, B., Fuller, R., Prevost, J., 2006. Development of a coupled geochemical transport code to simulate cement degradation in $CO_2$ saturated brine. Int. Conf. Greenh. Gas Control Technol. 19–22.

Huet, B.M., Prevost, J.H., Scherer, G.W., 2010. Quantitative reactive transport modeling of Portland cement in $CO_2$-saturated water. Int. J. Greenh. Gas Control 4, 561–574. https://doi.org/10.1016/j.ijggc.2009.11.003.

Iyer, J., Walsh, S.D.C., Hao, Y., Carroll, S.A., 2017. Incorporating reaction-rate dependence in reaction-front models of wellbore-cement/carbonated-brine systems. Int. J. Greenh. Gas Control 59, 160–171. https://doi.org/10.1016/j.ijggc.2017.01.019.

Jennings, H.M., Thomas, J.J., Gevrenov, J.S., Constantinides, G., Ulm, F.J., 2007. A multi-technique investigation of the nanoporosity of cement paste. Cem. Concr. Res. 37, 329–336. https://doi.org/10.1016/j.cemconres.2006.03.021.

Jeong, Y.J., Youm, K.S., Yun, T.S., 2018. Effect of nano-silica and curing conditions on the reaction rate of class G well cement exposed to geological $CO_2$-sequestration

conditions. Cem. Concr. Res. 109, 208–216. https://doi.org/10.1016/j.cemconres.2018.05.001.
Jurowski, K., Grzeszczyk, S., 2018. Influence of selected factors on the relationship between the dynamic elastic modulus and compressive strength of concrete. Materials (Basel) 11. https://doi.org/10.3390/ma11040477.
Kestin, J., Khalifa, E., Correia, R., 1981. Tables of the Dynamic and Kinematic Viscosity of Aqueous NaCl Solutions. J. Phys. Chem. Ref. Data. 10, 71–87.
Kuhn, H., Försterling, H.D., Waldeck, D.H., David, H., 2009. Principles of Physical Chemistry. John Wiley.
Kutchko, B.G., Strazisar, B.R., Dzombak, D.A., Lowry, G.V., Thauiow, N., 2007. Degradation of well cement by $CO_2$ under geologic sequestration conditions. Environ. Sci. Technol. 41, 4787–4792. https://doi.org/10.1021/es062828c.
Kutchko, B.G., Strazisar, B.R., Hawthorne, S.B., Lopano, C.L., Miller, D.J., Hakala, J.A., Guthrie, G.D., 2011. $H_2S$-$CO_2$ reaction with hydrated Class H well cement: acid-gas injection and $CO_2$ co-sequestration. Int. J. Greenh. Gas Control 5, 880–888. https://doi.org/10.1016/j.ijggc.2011.02.008.
Kutchko, B.G., Strazisar, B.R., Huerta, N., Lowry, G.V., Dzombak, D.A., Thaulow, N., 2009. $CO_2$ reaction with hydrated class H well cement under geologic sequestration conditions: effects of flyash admixtures. Environ. Sci. Technol. 43, 3947–3952. https://doi.org/10.1021/es803007e.
Kutchko, B.G., Strazisar, B.R., Lowry, G.V., Dzombak, D.a., Thaulow, N., 2008. Rate of $CO_2$ attack on hydrated class H well cement under geologic sequestration conditions. Environ. Sci. Technol. 42, 6237–6242. https://doi.org/10.1021/es800049r.
Lafhaj, Z., Goueygou, M., Djerbi, A., Kaczmarek, M., 2006. Correlation between porosity, permeability and ultrasonic parameters of mortar with variable water /cement ratio and water content. Cem. Concr. Res. 36, 625–633. https://doi.org/10.1016/j.cemconres.2005.11.009.
Lecampion, B., Vanzo, J., Ulm, F.-J., Huet, B., Germay, C., Khalfallah, I., Dirrenberger, J., 2011. Evolution of Portland cement mechanical properties exposed to $CO_2$-rich fluids: investigation at different scales. MPPS 2011. Symp. Mech. Phys. Porous Solids A Tribut. to Pr. Oliv. Coussy 1–24.
Lesti, M., Tiemeyer, C., Plank, J., 2013. $CO_2$ stability of Portland cement based well cementing systems for use on carbon capture & storage (CCS) wells. Cem. Concr. Res. 45, 45–54. https://doi.org/10.1016/j.cemconres.2012.12.001.
Li, Q., Lim, Y.M., Flores, K.M., Kranjc, K., Jun, Y.S., 2015. Chemical reactions of portland cement with aqueous $CO_2$ and their impacts on cements mechanical properties under geologic $CO_2$ sequestration conditions. Environ. Sci. Technol. 49, 6335–6343. https://doi.org/10.1021/es5063488.
Li, Y.H., Gregory, S., 1974. Diffusion of ions in sea water and in deep-sea sediments. Geochim. Cosmochim. Acta 38, 703–714.
Li, Y.X., Chen, Y.M., Wei, J.X., He, X.Y., Zhang, H.T., Zhang, W.S., 2006. A study on the relationship between porosity of the cement paste with mineral additives and compressive strength of mortar based on this paste. Cem. Concr. Res. 36, 1740–1743. https://doi.org/10.1016/j.cemconres.2004.07.007.
Liaudat, J., Martínez, A., López, C.M., Carol, I., 2018. Modelling acid attack of oilwell cement exposed to carbonated brine. Int. J. Greenh. Gas Control 68, 191–202. https://doi.org/10.1016/j.ijggc.2017.11.015.
Liu, B., Feng, X., Zhang, S.M., 2009. The effective Young's modulus of composites beyond the Voigt estimation due to the Poisson effect. Compos. Sci. Technol. 69, 2198–2204. https://doi.org/10.1016/j.compscitech.2009.06.004.
Lokhorst, A., Wildenborg, T., 2005. Introduction on $CO_2$ geological storage. Classification of storage options. Oil Gas Sci. Technol. 60, 513–515. https://doi.org/10.2516/ogst:2005033.
Lyons, W.C., Plisga, G.J., 2011. Standard Handbook of Petroleum and Natural Gas Engineering. Elsevier.
Manzanal, D., Pereira, J.M., 2013. Effects of the presence of $CO_2$ at the well/caprock interface: crystallization damage. Proc. Int. Conf. Offshore Mech. Arctic Eng. OMAE Nantes 1–6. https://doi.org/10.1115/OMAE2013-11543.
Mason, H.E., Frane, W.L.Du, Walsh, S.D.C., Dai, Z., Charnvanichborikarn, S., Carroll, S. A., 2013. Chemical and mechanical properties of wellbore cement altered by $CO_2$ - rich brine using a multianalytical approach. Environ. Sci. Technol. 47, 1745–1752. https://doi.org/10.1021/es3039906.
Matyka, M., Khalili, A., Koza, Z., 2008. Tortuosity-porosity relation in porous media flow. Phys. Rev. E - Stat. Nonlinear Soft Matter Phys. 78 https://doi.org/10.1103/PhysRevE.78.026306.
Merkel, C., Deuschle, J., Griesshaber, E., Enders, S., Steinhauser, E., Hochleitner, R., Brand, U., Schmahl, W.W., 2009. Mechanical properties of modern calcite-(Mergerlia truncata) and phosphate-shelled brachiopods (Discradisca stella and Lingula anatina) determined by nanoindentation. J. Struct. Biol. 168, 396–408. https://doi.org/10.1016/J.JSB.2009.08.014.
Moner-Girona, M., Roig, A., Molins, E., Martínez, E., Esteve, J., 1999. Micromechanical properties of silica aerogels. Appl. Phys. Lett. 75, 653–655. https://doi.org/10.1063/1.124471.
Moorehead, D.R., 1986. Cementation by the carbonation of hydrated lime. Cem. Concr. Res. 16, 700–708. https://doi.org/10.1016/0008-8846(86)90044-X.
Morandeau, A., Thiéry, M., Dangla, P., 2015. Impact of accelerated carbonation on OPC cement paste blended with fly ash. Cem. Concr. Res. 67, 226–236. https://doi.org/10.1016/j.cemconres.2014.10.003.
Morandeau, A., Thiéry, M., Dangla, P., 2014. Investigation of the carbonation mechanism of CH and C-S-H in terms of kinetics, microstructure changes and moisture properties. Cem. Concr. Res. 56, 153–170. https://doi.org/10.1016/j.cemconres.2013.11.015.
National Center for Biotechnology Information, 2022. PubChem Compound Summary for CID 10112, Calcium carbonate [WWW Document].
Omosebi, O., Maheshwari, H., Ahmed, R., Shah, S., Osisanya, S., Hassani, S., DeBruijn, G., Cornell, W., Simon, D., 2016. Degradation of well cement in HPHT acidic environment: effects of $CO_2$ concentration and pressure. Cem. Concr. Compos. 74, 54–70. https://doi.org/10.1016/j.cemconcomp.2016.09.006.
Perkins, T.K., Johnston, O.C., 1963. A review of diffusion and dispersion in porous media. Soc. Pet. Eng. J. 3, 70–84. https://doi.org/10.2118/480-PA.
Phani, K.K., Niyogi, S.K., 1987. Young's modulus of porous brittle solids. J. Mater. Sci. 22, 257–263. https://doi.org/10.1007/BF01160581.
Ringrose, Philip, 2020. How to Store $CO_2$ Underground: Insights from early-mover CCS Projects. Springer.
Phung, Q.T., Maes, N., Jacques, D., De Schutter, G., Ye, G., Perko, J., 2016. Modelling the carbonation of cement pastes under a $CO_2$ pressure gradient considering both diffusive and convective transport. Constr. Build. Mater. 114, 333–351. https://doi.org/10.1016/j.conbuildmat.2016.03.191.
Promentilla, M.A.B., Sugiyama, T., Hitomi, T., Takeda, N., 2009. Quantification of tortuosity in hardened cement pastes using synchrotron-based X-ray computed microtomography. Cem. Concr. Res. 39, 548–557. https://doi.org/10.1016/j.cemconres.2009.03.005.
Rebreanu, L., Vanderborght, J.P., Chou, L., 2008. The diffusion coefficient of dissolved silica revisited. Mar. Chem. 112, 230–233. https://doi.org/10.1016/j.marchem.2008.08.004.
Rezagholilou, A., Papadakis, V.G., Nikraz, H., 2017. Rate of carbonation in cement modified base course material. Constr. Build. Mater. 150, 646–652. https://doi.org/10.1016/j.conbuildmat.2017.05.226.
Rimmelé, G., Barlet-gouédard, V., Porcherie, O., Goffé, B., Brunet, F., 2008a. Heterogeneous porosity distribution in Portland cement exposed to CO 2 -rich fl uids. Cem. Concr. Res. 38, 1038–1048. https://doi.org/10.1016/j.cemconres.2008.03.022.
Rimmelé, G., Barlet-Gouédard, V., Porcherie, O., Goffé, B., Brunet, F., 2008b. Heterogeneous porosity distribution in Portland cement exposed to CO2-rich fluids. Cem. Concr. Res. 38, 1038–1048. https://doi.org/10.1016/j.cemconres.2008.03.022.
Šavija, B., Luković, M., 2016. Carbonation of cement paste: Understanding, challenges, and opportunities. Constr. Build. Mater. 117, 285–301. https://doi.org/10.1016/j.conbuildmat.2016.04.138.
Shah, V., Scrivener, K., Bhattacharjee, B., Bishnoi, S., 2018. Changes in microstructure characteristics of cement paste on carbonation. Cem. Concr. Res. 109, 184–197. https://doi.org/10.1016/j.cemconres.2018.04.016.
Shen, Q., Pan, G., Bao, B., 2016. Influence of CSH carbonation on the porosity of cement paste. Mag. Concr. Res. 68, 504–514. https://doi.org/10.1680/jmacr.15.00286.
Silva, A., Neves, R., De Brito, J., 2014. Statistical modelling of carbonation in reinforced concrete. Cem. Concr. Compos. 50, 73–81. https://doi.org/10.1016/j.cemconcomp.2013.12.001.
Steefel, C.I., Appelo, C.A.J., Arora, B., Jacques, D., Kalbacher, T., Kolditz, O., Lagneau, V., Lichtner, P.C., Mayer, K.U., Meeussen, J.C.L., Molins, S., Moulton, D., Shao, H., Šimůnek, J., Spycher, N., Yabusaki, S.B., Yeh, G.T., 2015. Reactive transport codes for subsurface environmental simulation. Comput. Geosci. https://doi.org/10.1007/s10596-014-9443-x.
Ta, V.L., Bonnet, S., Senga Kiesse, T., Ventura, A., 2016. A new meta-model to calculate carbonation front depth within concrete structures. Constr. Build. Mater. 129, 172–181. https://doi.org/10.1016/J.CONBUILDMAT.2016.10.103.
Taylor, H.F.W., 1997. Cement chemistry. T. Telford 123.
Trapote-Barreira, A., Cama, J., Soler, J.M., 2014. Dissolution kinetics of C-S-H gel: flow-through experiments. Phys. Chem. Earth 70–71, 17–31. https://doi.org/10.1016/j.pce.2013.11.003.
Ulm, F.J., Lemarchand, E., Heukamp, F.H., 2003. Elements of chemomechanics of calcium leaching of cement-based materials at different scales. Eng. Fract. Mech. 70, 871–889. https://doi.org/10.1016/S0013-7944(02)00155-8.
Urbonas, L., Leno, V., Heinz, D., 2016. Effect of carbonation in supercritical $CO_2$ on the properties of hardened cement paste of different alkalinity. Constr. Build. Mater. 123, 704–711. https://doi.org/10.1016/j.conbuildmat.2016.07.040.
Vallin, V., Pereira, J.M., Fabbri, A., Wong, H., 2013. Numerical modelling of the hydro-chemo-mechanical behaviour of geomaterials in the context of $CO_2$. Injection 3052–3069. https://doi.org/10.1002/nag.
Velez, K., Maximilien, S., Damidot, D., Fantozzi, G., Sorrentino, F., 2001. Determination by nanoindentation of elastic modulus and hardness of pure constituents of Portland cement clinker. Cem. Concr. Res. 31, 555–561. https://doi.org/10.1016/S0008-8846(00)00505-6.
Walsh, S.D.C., Du Frane, W.L., Mason, H.E., Carroll, S.A., 2013. Permeability of wellbore-cement fractures following degradation by carbonated brine. Rock Mech. Rock Eng. 455–464 https://doi.org/10.1007/s00603-012-0336-9.
Walsh, S.D.C., Mason, H.E., Du Frane, W.L., Carroll, S.A., 2014. Mechanical and hydraulic coupling in cement-caprock interfaces exposed to carbonated brine. Int. J. Greenh. Gas Control 25, 109–120. https://doi.org/10.1016/j.ijggc.2014.04.001.
Wang, X., Subramaniam, K.V., 2011. Ultrasonic monitoring of capillary porosity and elastic properties in hydrating cement paste. Cem. Concr. Compos. 33, 389–401. https://doi.org/10.1016/J.CEMCONCOMP.2010.11.001.
Wigand, M., Kaszuba, J.P., Carey, J.W., Hollis, W.K., 2009. Geochemical effects of $CO_2$ sequestration on fractured wellbore cement at the cement/caprock interface. Chem. Geol. 265, 122–133. https://doi.org/10.1016/j.chemgeo.2009.04.008.
Wolterbeek, T.K.T., Hangx, S.J.T., Spiers, C.J., 2016. Effect of $CO_2$-induced reactions on the mechanical behaviour of fractured wellbore cement. Geomech. Energy Environ. 7, 26–46. https://doi.org/10.1016/j.gete.2016.02.002.
Xu, B., Yuan, B., Wang, Y., Zeng, S., Yang, Y., 2019. Nanosilica-latex reduction carbonation-induced degradation in cement of $CO_2$ geological storage wells. J. Nat. Gas Sci. Eng. 65, 237–247. https://doi.org/10.1016/j.jngse.2019.03.013.

Xu, T., Sonnenthal, E., Spycher, N., Pruess, K., 2004. TOUGHREACT User's Guide: A Simulation Program for Non-isothermal Multiphase Reactive Geochemical Transport in Variably Saturated Geologic Media.

Yang, D.Y., Guo, R., 2014. Experimental study on modulus and hardness of ettringite. Exp. Tech. 38, 6–12. https://doi.org/10.1111/j.1747-1567.2011.00744.x.

Yuanhua, L., Dajiang, Z., Dezhi, Z., Yuanguang, Y., Taihe, S., Kuanhai, D., Chengqiang, R., Deping, Z., Feng, W., 2013. Experimental studies on corrosion of cement in $CO_2$ injection wells under supercritical conditions. Corros. Sci. 74, 13–21. https://doi.org/10.1016/j.corsci.2013.03.018.

Zhang, L., Dzombak, D.A., Nakles, D.V., Brunet, J.P.L., Li, L., 2013. Reactive transport modeling of interactions between acid gas ($CO_2$+$H_2S$) and pozzolan-amended wellbore cement under geologic carbon sequestration conditions. Energy Fuels 27, 6921–6937. https://doi.org/10.1021/ef401749x.

Zhang, M., Bachu, S., 2011. Review of integrity of existing wells in relation to $CO_2$ geological storage: What do we know? Int. J. Greenh. Gas Control 5, 826–840. https://doi.org/10.1016/j.ijggc.2010.11.006.

Zhu, H.X., Fan, T.X., Zhang, D., 2015. Composite materials with enhanced dimensionless Young's modulus and desired Poisson's ratio scientific reports. Nat. Publ. Group 1–8. https://doi.org/10.1038/srep14103.